

Quantitative Evaluation of Endoscopic SLAM

Methods: EndoSLAM Dataset

Kutsev Bengisu Ozyoruk, Kagan Incetan, Gulfize Coskun, Guliz Irem Gokceler, Yasin Almalioglu, Faisal Mahmood, Nicholas J. Durr, Eva Curto, Luis Perdigoto, Marina Oliveira, Helder Araujo, Henrique Alexandrino, Hunter B. Gilbert, and Mehmet Turan

Abstract—Deep learning techniques hold promise to improve dense topography reconstruction and pose estimation, as well as simultaneous localization and mapping (SLAM). However, currently available datasets do not support effective quantitative benchmarking. With this paper, we introduce a comprehensive endoscopic SLAM dataset containing both capsule and standard endoscopy recordings. A Panda robotic arm, two different commercially available high precision 3D scanners, two different commercially available capsule endoscopes with different camera properties and two different conventional endoscopy cameras were employed to collect data from eight ex-vivo porcine gastrointestinal (GI)-tract organs. In total, 35 sub-datasets are provided: 18 sub-datasets for colon, 12 sub-datasets for stomach and five sub-datasets for small intestine, while four of these contain polyp-mimicking elevations carried out by an expert gastroenterologist. To exemplify the use-case, SC-SfMLearner was comprehensively benchmarked. The codes and the link for the dataset are publicly available at <https://github.com/CapsuleEndoscope/EndoSLAM>. A video demonstrating the experimental setup and procedure is available at https://www.youtube.com/watch?v=G_LCe0aWWdQ.

Index Terms—Endoscopic SLAM dataset, Capsule endoscopy, Standard endoscopy, Deep learning, SLAM, Pose estimation, 3D map reconstruction, Computer vision.

I. INTRODUCTION

GASTROINTESTINAL cancers affect over 28 million patients annually, representing about 26% of the global cancer incidence and 35% of all cancer-related deaths [5],

(Corresponding Authors: Mehmet Turan and Helder Araujo. This work was supported by the Scientific and Technological Research Council of Turkey (TUBITAK) for 2232 - The International Fellowship for Outstanding Researchers)

Mehmet Turan, Kutsev Bengisu Ozyoruk, Kagan Incetan, Gulfize Coskun and Guliz Irem Gokceler are with the Institute of Biomedical Engineering, Bogazici University, Turkey {mehmet.turan, bengisu.ozyoruk, kagan.incetan, guliz.gokceler}@boun.edu.tr, gulfizecoskun@marun.edu.tr

Yasin Almalioglu is with the Computer Science Department, University of Oxford, Oxford, UK yasin.almalioglu@cs.ox.ac.uk

Faisal Mahmood is with the Department of Pathology, Harvard Medical School, Boston, MA faisalmahmood@bwh.harvard.edu

Nicholas J. Durr is with the Department of Biomedical Engineering, Johns Hopkins University, Baltimore, MD ndurr@jhu.edu

Helder Araujo, Eva Curto, Luis Perdigoto, Marina Oliveira are with the Institute for Systems and Robotics, University of Coimbra, Portugal {helder@isr.uc.pt, evarcurto@gmail.com, luis.perdigoto@ipleiria.pt, marinaa.oliveira95@gmail.com}

Henrique Alexandrino is with Faculty of Medicine, Clinical Academic Center of Coimbra, University of Coimbra, Coimbra, Portugal halalexandrino123@gmail.com

Hunter B. Gilbert is with the Department of Mechanical and Industrial Engineering, Louisiana State University, Baton Rouge, LA, USA hbgilbert@lsu.edu



Fig. 1: Experimental setup. The pre-harvested and cleaned porcine colons were cut and sewn to an L-shaped, Z-shaped scaffold by a health practitioner. For data transfer between the receiver and wireless capsule endoscope(WCE), a data belt, copper wiring and wireless transmitter were used. A special holder for the capsule was designed, 3D printed (see Fig. 7 b) and attached to the robot arm (see Fig. 7 a). The dataset was recorded in dark room.

[6]. Besides, GI cancer is the second deadliest cancer type with reported 3.4 million GI related deaths globally in 2018 [6]. Direct visual inspection(DVI) of these cancers is the simplest and most effective technique for screening. Esophagogastroduodenoscopy (EGD) and colonoscopy are used to visualize gastrointestinal diseases specifically in colon and

TABLE I: **Dataset Survey.** An overview of existing datasets for disease classification, polyp recognition, segmentation, pose, tracking and depth estimation. The size of each dataset in terms of number of images, and corresponding organs are also listed. The datasets, collected via capsule endoscopy, standard endoscopy and laparoscopy, are denoted with $^{\diamond}$, † and * , respectively.

Dataset Name	Findings	Organs	Tasks	Size
Kvasir-SEG †	Polyps	Colon	Segmentation	1,000
Kvasir † [1]	Z-line, pylorus, cecum, esophagitis, polyps, ulcerative colitis, dyed	Colon	Disease detection	6,000
	Lifted polyps and dyed resection margins	Colon	Segmentation	2,000
Hamlyn Centre Datasets †*	Polyp	Colon	Segmentation	7,894
	-	Kidney	Disparity	40,000
	Polyp	Colon	Polyp recognition Localisation	2,000
	-	Liver, ureter, kidney, abdomen	Tissue deformation Tracking	-
KID Dataset $^{\diamond}$ [2]	Angioectasias, apthae, chylous cysts and polypoid, vascular and inflammatory lesions	Small Bowel and colon	Classification	2,448
NBI-InFrames † [3]	Angioectasias, apthae, chylous cysts and polypoid	Larynx	Classification	720
EndoAbs † [4]	-	Liver, kidney, spleen	Classification	120
ASU-MAYO Clinic †	Polyp	Colons	Segmentation	18,902
ROBUST-MIS Challenge *	Rectal cancer	Abdomen	Segmentation	10,040

rectum while capsule endoscopy (CE) is preferred for small bowel exploration [7]. According to the Survey of Endoscopic Capacity (SECAP), an estimated 15 million colonoscopies were performed in 2012 [8].

Specifically, the malignant tumors developed in the small intestine like Adenocarcinoma, Intestinal Lymphoma, Leiomyosarcoma or metastatic malignancy from lung or breast are deadly diseases. Polyposis syndromes involving the small bowel include Familial Adenomatous Polyposis, generalized Juvenile polyposis, Peutz-Jeghers and Cronkhite-Canada syndromes, of which Familial Adenomatous Polyposis is the most deadly. The diagnosis of these polyps and small-bowel tumors is challenging due to the rarity of lesions, lack of common symptoms across patients, and variety of the symptoms [9]. In these cases, differential diagnosis from blood tests and symptoms alone is not sufficient, and visual examination through capsule endoscopy can provide valuable information.

After visual confirmation of any feature of diagnostic importance, the natural next question is “where is it?”. This question has motivated the development of localization techniques and systems for capsule endoscopes. Techniques that have been explored based on added sensors include RF-based signal triangulation [10], received signal strength-based localization [11], magnetic tracking [12], x-ray [13], positron emission markers [14], and others [15]. Since visualization is already provided in capsule endoscopes, the development of vision-based odometry and simultaneous localization and mapping (SLAM) systems is also of significant interest, either to remove the need for added hardware for pose sensing or to provide

additional information for 3D tracking. While current capsules are propelled by the natural peristaltic motion of the GI tract, active capsule endoscopes may one day provide drug delivery, biopsy, and surgical functions [16], and vision-based SLAM will be critical to enabling these functions and other forms of complementary situational awareness including, for example, decision support and augmented reality [17].

A variety of computer vision techniques are available to provide 3D reconstruction and mapping of surgical scenes and endoscope localization. In the work of Mountney et al. [18], a vSLAM method is used with an Extended Kalman Filter SLAM (EKF-SLAM) framework to generate localization and soft tissue mapping where sequential frames acquired by moving stereo endoscopes are used to 6 DoF (Degree of Freedom) camera pose information. In robotic surgical systems such as da VinciTM, real-time 3D reconstruction methods have been applied and validated on phantom models [19], [20]. Lin et al. in [20] adopt and extend Parallel Tracking and Mapping (PTAM) method to detect deformations on a non-rigid phantom to create 3D reconstruction of intestine model and to track endoscope position and orientation. Some other works are focused on more commonly used monocular endoscopes. Mirota et al. [21] generate a 3D reconstruction from endoscope video during sinus surgeries by using feature detection and registered data from CT scan tracking endoscope location. In [22], another monocular vSLAM method is used to provide real-time 3D map of the abdominal cavity for hernia repair interventions. Apart from standard endoscopes, vSLAM

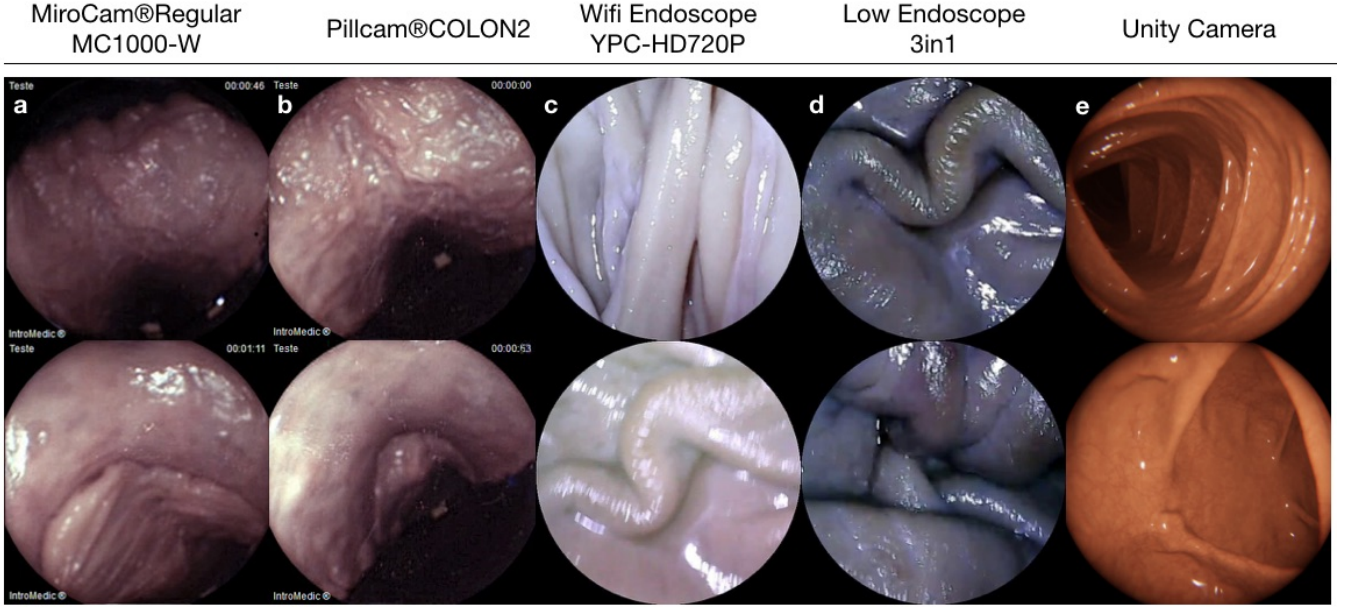


Fig. 2: **Selection of recorded images.** **a** was collected by MiroCam capsule endoscope **b** was acquired by the frontal camera of a PillCam capsule **c** was acquired by the HighCam **d** was acquired by the LowCam, and **e** is synthetically generated data using Unity environment. Lack of large annotated real endoscopic images has motivated us to build an anatomically realistic colon simulation. Since the dataset is composing real and simulated frames, it is convenient to develop domain adaptation algorithms.

techniques have also been used in capsule endoscopy [23], [24].

A robust and reliable SLAM module is critical for next-generation capsule robots, but several technical challenges make this need difficult to meet. Capsule endoscope cameras have low frame rate and low resolution due to space limitations, which strongly challenges SLAM methods. Difficulties in feature extraction and outlier removal, reflections due to organ fluids and peristaltic motions are further examples of inherent challenges. Accurate and reliable vSLAM methods are necessary to overcome these issues to enable advanced next-generation active capsule endoscopy functionalities including biopsy, drug delivery and automated polyp detection. To overcome challenges of repetitive textures, Turan et al. [25]–[27], used deep learning based approaches for depth estimation, 3D reconstruction of a phantom, and real-time pose tracking. Those challenges have motivated the exploration of data-driven machine and deep learning based approaches that eschew complex models.

However, the development of algorithms based on machine learning and, in particular, on deep learning, require large amounts of data. For endoscopic images, one recent study required on the order of tens of thousands of image frames [26]. Public datasets can accelerate development by enabling a broader research community to work on the problem [1], [28], [29]. Several datasets are available in the context of endoscopy, which are summarized in Table I (Further details are available in Appendix B).

However, the existing datasets do not fully support the development of endoscopic SLAM methods, because they lack ground-truth odometry and 3D map reconstructions. To fill this

void, we have created a dedicated dataset designed for the development of 6-DoF pose estimation and fully dense 3D map reconstruction methods. We introduce the EndoSLAM dataset, recorded using multiple endoscopic cameras and ex-vivo porcine GI organs belonging to different animals. The experimentally collected dataset is designed to meet the following major requirements for scientific research and development of endoscopic SLAM methods:

- Time-synchronized, ground-truth 6 DoF pose data
- High precision, ground-truth 3D reconstructions
- Multiple organs from multiple individuals
- Images from cameras with differing intrinsic properties
- Image sequences with differing native frame rates
- Images under a variety of lighting conditions
- Distinguishable features of diagnostic significance (e.g. presence/absence of polyps).

In addition to the experimentally collected data, synthetically generated data from a 3D simulation environment is included to facilitate study of the simulation to real-world domain-transfer problems.

Section II describes the experimental setup and gives details about the specifications of the devices used for dataset recording. Section III introduces the dataset and the details of collection procedure. Section IV exemplifies the use of the dataset by examining performance of state-of-the-art vision-based localization and mapping with SC-SfMLearner and fully dense 3D map reconstruction via a traditional pipeline. Finally, Section V offers concluding remarks.

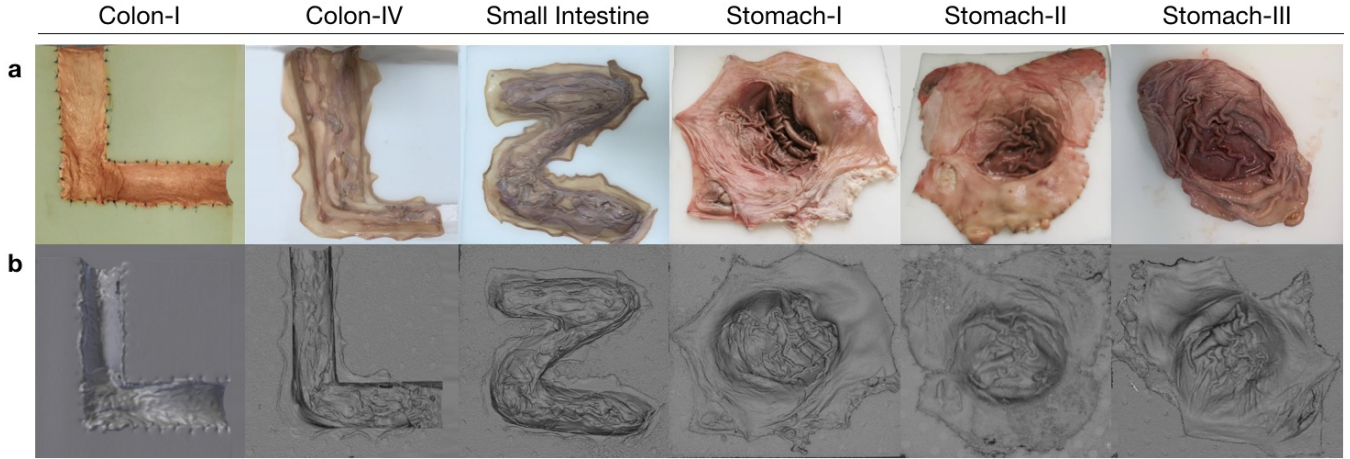


Fig. 3: **3D-Scanner Images for EndoSLAM Dataset.** 3D-scanner images obtained for six organs which are fixed to scaffolds that were cut in O, Z and L shapes to mimic the GI-tract path through the ascending colon to the transverse colon. Gathering point cloud data from two colon, one intestine and three stomach from different individuals make dataset appropriate for transfer learning algorithms. Besides, the algorithm performance on the tissue with various texture details for the same organ type can be tested. **a** shows RGB images of organs **b** shows corresponding 3D reconstruction from .ply files for organs recorded via 3D Scanner.

II. SETUP

The experimental setup was specifically designed to support the collection of endoscopic video, accurate 6 DoF ground truth pose, organ shape and topography data. The essential components are four endoscopic video cameras (see Fig. 7i, j, l, m in Appendix A), a robot arm to track the trajectory and quantify the pose values (see Fig. 7a), and high precision 3D scanners for ground truth organ shape measurement (see Fig. 7g-h). All other equipment are also illustrated in Fig. 7.

For camera devices, we used MiroCam[®] (see Fig. 7m) and Pillcam[®] COLON2 (see Fig. 7l) capsule endoscope cameras and two other cameras (HighCam and LowCam) representative of conventional endoscopy cameras (see Fig. 7i-j). Their specifications are as follows:

- MiroCam[®] Regular MC1000-W endoscopic video capsule: 320×320 image resolution, 3 fps frame rate, 170° field of view, 7 - 20 mm depth of field, 6 white LED's (Fig. 7m). [30]
- Pillcam[®] COLON2 double endoscopic camera capsule: 256×256 each camera, 4 fps to 35 fps variable frame rate, 344° field of view (172° each camera), 4 LEDs (each camera), Fig. 7l [30].
- High Resolution Endoscope Camera (YPC-HD720P): 1280×720 image resolution, 20 fps frame rate, 70° field of view, 4-6 cm depth of field, 6 adjustable white LEDs, Fig. 7i.
- Low Resolution Endoscope 3 in 1 Camera: 640×480 image resolution, 20 fps frame rate, 60° field of view, 3-8 cm depth of field, 6 adjustable LEDs, Fig. 7j.

In the rest of the paper, we will call MiroCam[®] Regular MC1000-W endoscopic video capsule as MiroCam, Pillcam[®] COLON2 as PillCam, High Resolution Endoscope Camera (YPC-HD720P) as HighCam and Low Resolution Endoscope 3 in 1 Camera as LowCam for brevity.

To provide trajectory stabilization and ground-truth pose recording of the camera motions, Franka Emika Panda robotic arm was used. The robot controls the motion of the cameras (see Fig. 7a and Table II for critical performance specifications). The robot is employed in hand-guided mode and provides trajectory pose recording at high-frequency, 1 kHz.

TABLE II: Performance specifications of the Panda robotic arm.

Specification	Value
Degrees of freedom	7
Payload	3 kg
Reach	855 mm
Pose repeatability (ISO 9283)	0.1 mm
Path deviation	1.25 mm
Cartesian velocity limit	2 m s ⁻¹

Ground truth geometries of the organs were acquired via two commercially-available 3D scanners, the Artec 3D Eva and Shining 3D Einscan Pro 2x (see Fig. 7g and h in Appendix A). 3D models of organs were reconstructed as in Fig. 3 and the depth distributions for corresponding organs are denoted in Fig. 15 Appendix F. Relevant performance specifications of the 3D scanners are as follows:

- Artec 3D Eva: ± 0.5 mm 3D resolution, ± 0.1 mm 3D point accuracy, $\pm 0.03\%$ 3D accuracy over 100 cm distance [31].
- Shining 3D EinScan Pro 2x: 0.2-2mm point distance; ± 0.5 mm 3D resolution, ± 0.05 mm 3D point accuracy, $\pm 0.03\%$ 3D accuracy over 100 cm distance [32].

III. DATASET COLLECTION

The ex-vivo part of dataset consists of a total of 42,700 frames. Of these, 21,428 images are from the HighCam,

TABLE III: **Quantitative results of pose prediction for various organs and trajectories.** Unsupervised pose estimation algorithm SC-SfMLearner [33] is evaluated using ATE and translational and rotational RPE metrics. The results are listed for six trajectories in three organs using HighCam and LowCam. Since Model-I trained fully with ex-vivo data and Model-III is fine-tuned with the same dataset, we observe increase in rotational error compared to Model-II for both HighCam and LowCam trajectories. The underlying reason for that is motivated by difficulty in creating rotations by manually guided robotic arm.

Organ, Trajectory		Trajectory Length [m]	ATE (mean \pm std) [m]	Trans. RPE (mean \pm std) [m]	Rot. RPE (mean \pm std) [deg]	Trajectory Length [m]	ATE (mean \pm std) [m]	Trans RPE (mean \pm std) [m]	Rot RPE (mean \pm std) [deg]
HighCam					LowCam				
Model-I	Colon-IV,Traj-I	0.4286	0.1322 \pm 0.1071	0.0039 \pm 0.0041	2.4788 \pm 1.5027	0.6785	0.2156 \pm 0.1927	0.0037 \pm 0.0093	2.1031 \pm 2.2399
	Colon-IV,Traj-V	1.2546	0.7324 \pm 0.6611	0.0106 \pm 0.0264	4.2886 \pm 4.5207	1.1698	0.1777 \pm 0.1428	0.0046 \pm 0.0035	3.23 \pm 1.6579
	Intestine,Traj-I	1.2028	0.1692 \pm 0.1345	0.0038 \pm 0.0028	2.631 \pm 2.0552	0.8460	0.6115 \pm 0.544	0.0113 \pm 0.0228	4.884 \pm 4.0571
	Intestine,Traj-IV	1.0557	0.2113 \pm 0.2224	0.0754 \pm 0.1394	4.3084 \pm 5.4026	0.8265	0.192 \pm 0.147	0.0437 \pm 0.0406	2.9847 \pm 2.6123
	Stomach-III,Traj-I	1.1391	0.0981 \pm 0.083	0.0399 \pm 0.042	2.9931 \pm 3.1799	1.1621	0.2027 \pm 0.1433	0.0645 \pm 0.0663	4.1924 \pm 2.548
	Stomach-III,Traj-II	1.2948	0.1403 \pm 0.1174	0.0369 \pm 0.033	2.77 \pm 2.5883	1.3883	0.2174 \pm 0.1696	0.0516 \pm 0.0658	3.544 \pm 2.1604
Model-II	Colon-IV,Traj-I	0.4286	0.1287 \pm 0.0889	0.0012 \pm 0.0028	0.9385 \pm 0.6896	0.6785	0.2022 \pm 0.1626	0.0013 \pm 0.0060	0.6467 \pm 1.4119
	Colon-IV,Traj-V	1.2547	0.2054 \pm 0.1734	0.0024 \pm 0.0029	1.2452 \pm 0.965	1.1699	0.1667 \pm 0.1263	0.0021 \pm 0.003	1.2188 \pm 0.7715
	Intestine,Traj-I	1.2028	0.1700 \pm 0.1329	0.0012 \pm 0.0008	0.9450 \pm 0.7417	0.8460	0.1302 \pm 0.1167	0.0013 \pm 0.0008	1.0348 \pm 0.6951
	Intestine,Traj-IV	1.0557	0.1247 \pm 0.1327	0.0015 \pm 0.0009	0.9257 \pm 0.584	0.8265	0.0908 \pm 0.0819	0.0016 \pm 0.0009	0.8989 \pm 0.7854
	Stomach-III,Traj-I	1.1391	0.1670 \pm 0.1311	0.0016 \pm 0.0025	0.8014 \pm 0.8400	1.1621	0.1680 \pm 0.1445	0.0019 \pm 0.0011	1.0627 \pm 0.7417
	Stomach-III,Traj-II	1.2948	0.1729 \pm 0.1448	0.0021 \pm 0.0038	1.0683 \pm 1.1406	1.3883	0.1835 \pm 0.1675	0.0020 \pm 0.0010	1.1821 \pm 0.7631
Model-III	Colon-IV,Traj-I	0.4286	0.1304 \pm 0.1064	0.0043 \pm 0.0042	2.6624 \pm 1.6822	0.6785	0.1946 \pm 0.1708	0.0037 \pm 0.0092	2.0718 \pm 2.3018
	Colon-IV,Traj-V	1.25547	0.5849 \pm 0.5201	0.0092 \pm 0.0175	4.4083 \pm 4.6309	1.1698	0.2094 \pm 0.1613	0.005 \pm 0.0041	3.1999 \pm 1.8304
	Intestine,Traj-I	1.2028	0.1615 \pm 0.1351	0.0038 \pm 0.003	2.4716 \pm 1.9343	0.8459	1.2483 \pm 1.1257	0.0155 \pm 0.0426	4.5832 \pm 3.8278
	Intestine,Traj-IV	1.0557	0.2119 \pm 0.2022	0.0083 \pm 0.016	3.9877 \pm 5.2134	0.8264	0.2387 \pm 0.1675	0.0048 \pm 0.005	2.7019 \pm 2.189
	Stomach-III,Traj-I	1.1391	0.1139 \pm 0.1005	0.005 \pm 0.0054	2.8593 \pm 3.0514	1.1621	0.1226 \pm 0.0989	0.007 \pm 0.005	4.1709 \pm 2.3479
	Stomach-III,Traj-II	1.2948	0.1775 \pm 0.1335	0.0052 \pm 0.0039	2.7779 \pm 2.3914	1.3883	0.5052 \pm 0.3349	0.0066 \pm 0.0248	3.5363 \pm 2.5818

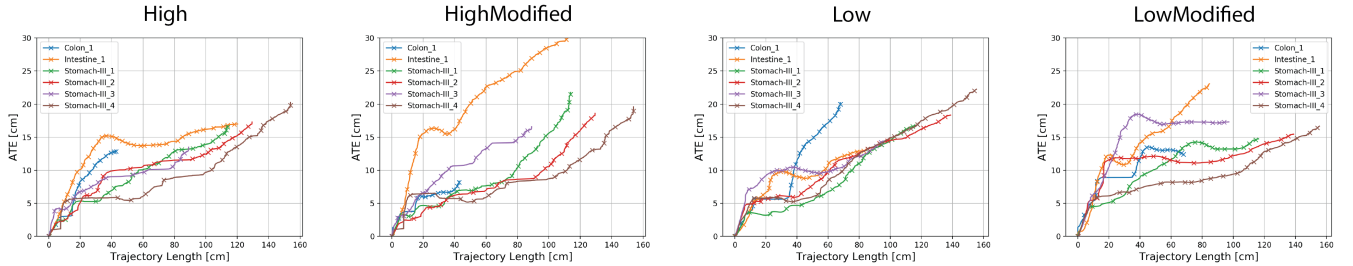


Fig. 4: **Absolute Trajectory Error (ATE) results with respect to traveled distance for six trajectories.** Errors are computed as the results of SC-SfMLearner, trained with synthetic data and evaluated on real images. The errors are shown for six different trajectories in three organs, using four image sequences of HighCam, LowCam, and the augmented data generated from each of those cameras). In the majority of cases, ATE for the modified images is higher than original counterpart.

17,978 images are from the LowCam, 239 images are from the PillCam and 3,055 images are from the MiroCam. The reader is referred to Fig. 2 and Fig. 13 in Appendix F for the illustration of recorded frames. Fig. 12 in Appendix E illustrates the overall data tree structure. Frames folders contain recorded endoscopic images in a given trajectory and Table X in Appendix F summarizes the trajectory classes for each organ. Trajectories for each organ can be found in the folder Poses in (.csv) and (.txt) format with 6 DoF pose coordinates: four orientation parameters (x; y; z; w) in quaternions and three absolute position parameters (x; y; z) in meters. Calibration folder contains intrinsic-extrinsic

calibration data of cameras in mat extensions and calibration sessions. 3D_Scanners folder consists of reconstructed 3D figures and point cloud data for six organs with a size of 23.2 GB in total.

A. Experimental Procedure

'L'-shaped, 'Z'-shaped semi-cylindrical and 'O' shaped semi-spherical scaffolds were cut in rectangular high-density solid foams with dimensions $30 \times 30 \times 17$ cm to be used as substrate for colons, small intestine and stomachs, respectively. The shape for colons mimics the GI-tract path through the ascending colon to the transverse colon. Cleaned porcine

organs were cut and sewn to the foam by a practitioner (Fig. 1) [34], [35]. All the capsules require a specific recorder to be worn by the patient. PillCam and MiroCam differ in multiple features and, in particular, PillCam transmits video wirelessly whereas MiroCam transmits video via a wired connection. For both PillCam and MiroCam, the capsules are placed into a 3D-printed, non-conducting holder attached to the robotic arm. HighCam and LowCam were also used in place of the capsule cameras to record endoscopic images in a similar set-up but with different organs, Colon-IV, Small Intestine, Stomach-I, Stomach-II, and Stomach-III, which are sewn on white scaffold.

All the recordings were made in a dark room with green and white background colored solid foams to create luminance and color contrast between the GI tract and environment. The orientations of the cameras (capsule and conventional) throughout the procedure are mostly along the longitudinal axis of the semi-cylindrical and semi-spherical surfaces. In most of the trajectories the capsule endoscopes do not touch the tissue, and all cameras never touch the tissue for all trajectories. In all the experiments the robot end-effector was driven by hand, with speeds ranging mostly between 16.76 mm/s to 25.97 mm/s with a peak speed of 286.68 mm/s and with accelerations mostly ranging from 279.254 mm/s² to 519.361 mm/s² with a peak acceleration of 14,680.15 mm/s². Alternating speed and accelerations are quite important in terms of SLAM evaluations, since performance of SLAM methods in general are significantly dependent on the complexity of the benchmark trajectories. For further quantitative analysis of robot motion, see Table VIII, IX in Appendix F.

Calibration of the experimental equipment includes camera intrinsic model parameters, the hand-eye transformation from robot to camera, and temporal synchronization between the camera frames and robot pose measurements. Each camera was calibrated against a pinhole camera model with non-linear radial lens distortion using MATLAB's Camera Calibration App (version R2020a), using the model from Zhang [36]. The hand-eye transformation between the robot end-effector coordinate frame and the camera frame was estimated with the procedure of Tsai and Lenz [37]. Finally, temporal synchronization was performed by correlating camera motion computed by optical flow with velocity measurements from the robot. Further details of the calibration procedures are given in Appendix C and D.

B. Dataset Augmentation

For the purpose of studying the robustness of SLAM algorithms, the set of experimentally obtained images is augmented by applying image transformations that reduce the quality of the data. The new images are provided separately from the originals in the dataset. The transformations that are applied include resizing, gaussian blur, fish-eye distortion, depth-of-field simulation using shift-variant defocus blurring, and frame dropping. The resize, vignetting and gaussian blur transformations are implemented with the opencv-python library (version 4.2.0.32), fish-eye distortion with the Pygame library (version 1.9.6), and depth-of-field with Matlab (version

R2020a) [38]. All codes for dataset augmentation are included in <https://github.com/CapsuleEndoscope/EndoSLAM> and the effect added images are exemplified in Fig. 14 Appendix F.

C. Synthetic Data Generation

In addition to real EndoSLAM dataset, we generated synthetic capsule endoscopic images with the use of a simulated environment in the Unity physics engine. The purpose of this additional data is to facilitate study of simulation-to-real transfer of learning-based algorithms in the context of endoscopic capsules. The geometry of the simulated environment was collected from anonymized computed tomography x-ray (CT) DICOM files and real endoscopic capsule videos. The CT images were converted into 3D models by using InVesalius, a free software that reconstructs CT and MR images into meshed 3D models [39]. The texture was applied to the 3D model by UV unwrapping a texture image on the meshes, that is created in Photoshop by making a flat mucosa image from a real endoscopy image, the purpose is that real endoscopy images can't be used since there are varying depths, shadows and dark areas due to the capsule's illumination and reflections. All these features that were removed from the real endoscopy image will be present in our environment, as we introduce a wet reflection surface to our organ models and an illumination source that will mimic the reflections and the other features. Finally, to make the synthetic images more photo-realistic, cinematic rendering, distortion effects (fish-eye distortion, chromatic aberration, vignette) and camera intrinsic parameters from real capsule endoscopes (Pillcam SB3 capsule endoscope) were applied to the rendering pipeline. Operating the virtual capsule inside the virtual 3D GI tract, we recorded an endoscopic video that contains 7,664 frames with pixel size of 360x360.

IV. DATASET USE-CASE AND EVALUATIONS

To illustrate the use-case of the dataset, we evaluated state-of-the-art methods for camera pose estimation and 3D reconstruction. The SC-SfMLearner algorithm [33], a recently proposed learning-based structure-from-motion method was benchmarked on the EndoSLAM dataset. Additionally, we designed and tested a traditional and fully dense 3D-reconstruction pipeline based on SIFT feature-matching and non-lambertian surface reconstruction for 3D-reconstruction. Error metrics that were used to quantitatively assess the performance of the algorithms are introduced in the following subsections.

A. Error Metrics

The SC-SfMLearner algorithm is tested versus the ground-truth data based on two metrics: absolute trajectory error (ATE) and relative pose error (RPE). The 3D-reconstruction is evaluated with surface reconstruction error. These error metrics are defined as follows based on the estimated and ground truth trajectories represented by $\mathbf{P}_1, \dots, \mathbf{P}_n \in \text{SE}(3)$ and $\mathbf{Q}_1, \dots, \mathbf{Q}_n \in \text{SE}(3)$, respectively, where the lower subscript is the time index and $\text{SE}(3)$ is the Special Euclidean Group

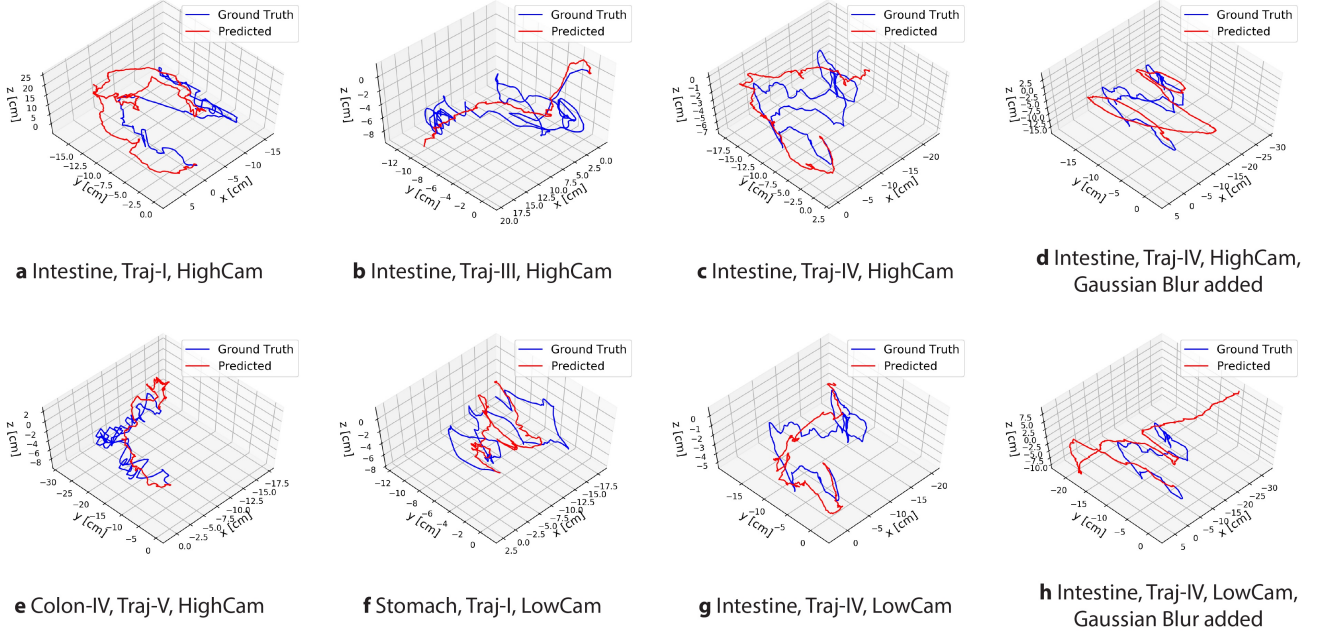


Fig. 5: **Qualitative results of pose estimation for eight tests.** The unsupervised pose prediction algorithm SC-SfMLearner is trained with synthetic data (Model-II) and the predicted pose results are aligned and plotted with their corresponding ground truth. For the fourth trajectory (Traj-IV) of small intestine, the results on blur effect added images with parameters $\alpha=3$, $\beta=3$, $\gamma=1$ (d and h) exhibits the adverse effect of adding post-processing distortions which then yields less prediction performance compared to the original recordings. The tested algorithm tracks loopy sections of the trajectories for most of the cases but predicted trajectories often fail to overlap with their ground truth counterparts, leaving offset in between.

in three dimensions. The robotic ground truth time series data is downsampled to the camera frame rate, which varies based on the camera.

1) *Absolute trajectory error (ATE)*: The ATE is a measure of global consistency between two trajectories, comparing absolute distances between ground truth and predicted poses at each point in time. Let the rigid body transformation \mathbf{S} be the best (least-squares) alignment of the trajectories [40]. Then absolute trajectory error for the i^{th} pose sample is calculated as follows:

$$ATE_i = \|\text{trans}(\mathbf{Q}_i^{-1} \mathbf{S} \mathbf{P}_i)\|. \quad (1)$$

The overall error throughout trajectory is defined by the root mean square of ATE_i .

2) *Relative Pose Error (RPE)*: Relative pose error measures the difference in the change in pose over a fixed length Δ between two trajectories. Defining $\mathbf{E}_i(\Delta) = (\mathbf{Q}_i^{-1} \mathbf{Q}_{i+\Delta})^{-1} (\mathbf{P}_i^{-1} \mathbf{P}_{i+\Delta})$, the translational and rotational RPE are given by:

$$\text{Trans RPE}_i(\Delta) = \|\text{trans}(\mathbf{E}_i)\|, \quad (2)$$

$$\text{Rot RPE}_i(\Delta) = \angle(\text{rot}(\mathbf{E}_i)), \quad (3)$$

where $\text{rot}(\mathbf{E}_i)$ is the rotation matrix of \mathbf{E}_i and $\angle(\cdot)$ is the positive angle of rotation. The errors are reported for $\Delta = 1$.

3) *Surface Reconstruction Error*: We use the map benchmark methodology proposed by [41] in order to evaluate the surface reconstruction quality. As the first step, one line segment manually identified between the reconstructed and ground truth 3D map. The match points are used to coarsely

align both maps. This coarse alignment is used as an initialization for the iterative closest point (ICP) algorithm. ICP iteratively aligns both maps until a termination criteria of 0.001 cm change in RMSE is reached.

B. Pose Estimation with SC-SfMLearner

Three models were trained using the EndoSLAM dataset, hereinafter referred to as Model-I, Model-II, and Model-III. Model-I was trained using three trajectories of Colon, Small Intestine, Stomach-I and two trajectories of Stomach-II. 11,314 and 1,577 images were randomly selected for training and validation, respectively. 200 epochs with batch size of four images were used to train the model with 18 ResNet layers. Model-II was trained with the synthetically generated colon images in the Unity simulation environment, where 2,039 and 509 frames were used for training and validation respectively. 210 epochs with a batch size of four images were used to train the model with 18 ResNet layers. Model-III is a fine-tuned version of Model-II, for which the training set of first model were used to fine-tune the model. Performances of Model-I, Model-II and Model-III are benchmarked in terms of ATE, translational RPE, and rotational RPE for the data recorded via the HighCam and LowCam. The results in Table III show clear advantage of fine-tuning Unity trained model with real ex-vivo dataset. The reader is referred to Table XI in Appendix G for the performance analysis of same models on the image modified versions. In the majority of Stomach-III results for both HighCam and LowCam, Model-I and Model-III achieve

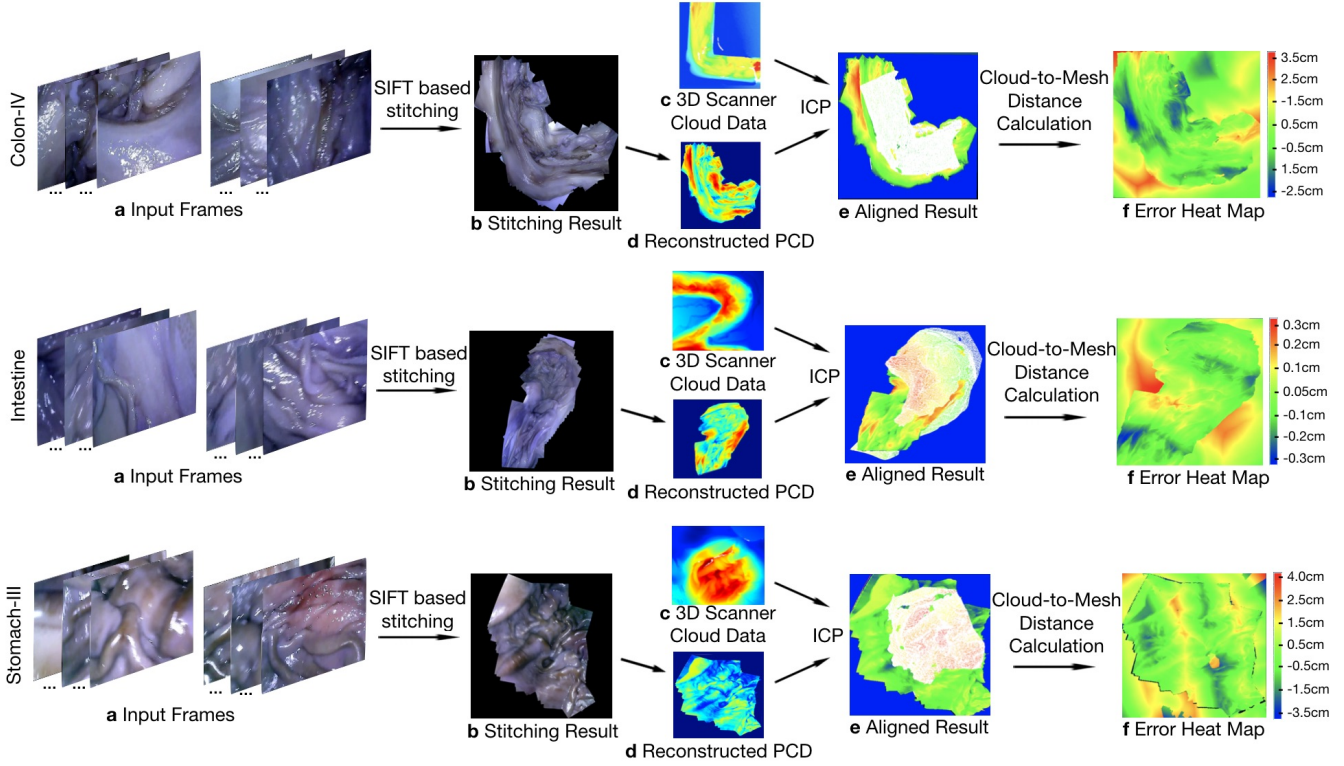


Fig. 6: 3D Reconstruction and Evaluation Pipeline. **a** shows input image sequences from Colon-IV, Small Intestine and Stomach-III trajectories which were downsampled to 4 fps and given as input to Scale Invariant Feature Transform (SIFT), separately. **b** shows the final stitched image which was formed by aligning and blending all input images. Specularities are suppressed using inpainting function of OpenCV. **c** shows 3D scanner point cloud data for each organ in ply-format. **d** shows pixel-wise depth values for inpainted images which were predicted using shape from shading. **e** shows the matched area between reference and aligned cloud points by emphasizing in white colour. Iterative Closest Point(ICP) was used to align the ground truth data and reconstructed surface after manually labelling a common line segment. **f** shows the cloud mesh distances in the form of heatmap with the bar displaying the root mean square error in cm. The RMSE values for Colon-IV, Small Intestine and Stomach-III are 1.09 cm, 1.02 cm and 1.11 cm, respectively.

better performance than Model-II which can be related to the fact that images from same organ type, Stomach-I and Stomach-II were used during training. In case of Model-III where the SC-SfMLearner model is fine-tuned on top of Model-II, predicted trajectories aligned with ground truth in general better than other models. This is an expected result as the training data for this model is the largest as well as the most diverse in terms of the depicted organ tissue.

Plots in Fig. 4 analyses RMSE results of Model-II with respect to traveled distances for six different trajectories recorded by HighCam and LowCam in the absence or presence of post processing effects. The figure shows that the more the trajectory is covered the higher drift occurs between ground truth and predicted trajectories. Moreover, the figure also reveals the adverse effect of including aforementioned effects with higher and more aggressively by increasing ATE score for the majority of cases. Finally, qualitative results are given in Fig. 5, which shows ground truth and predicted trajectories for eight test cases. It is seen that the trained model output generally follows the shape of the ground truth, but that substantial errors are present in all test cases.

Descriptive analysis of the camera speeds and accelerations

are shown in Fig. 16, Table VIII and Table IX in Appendix F. Since the robot motions are highly effective on image quality, we expect decrease in the pose estimation accuracy for the trajectories of Stomach-III which have highest mean speed and acceleration. The fact pave the way for the difficulty in alignment of those trajectories and also stitching of those frames.

As a further analysis, we have investigated if Gaussian blur and fish eye filtering of input images are correlated with model performances. Final ATE, rotational and translational RPE scores on varying levels of additional blur are depicted in Table XIII and Table XV in Appendix G. Similarly, errors on different radial distortion levels are depicted in Table XII and Table XIV in Appendix G. We applied Wilcoxon Signed Rank Test to analyze if the pose estimation performance of the models on various image sharpness and radial distortion levels significantly differ from each other. Although no statistically significant difference is achieved in terms of ATE on all distortion levels of Fish-eye and Gaussian blur effects for Model-I,II,III, we observed the significant difference($p < 0.05$) almost between all compared groups of radially distorted images in terms of rotational RPE for all models. The final

p-scores imply that there is no clear correlation between Gaussian blur and pose estimation up to a certain degree. Statistical significance is not reached proven by the fact that majority of the p-values are higher than 0.05, see Table XVI in Appendix H. However, there is strong evidence ($p < 0.05$) for the correlation of orientation estimation and fish-eye distortion, see Table XVII in Appendix H.

C. 3D Reconstruction Pipeline

3D reconstruction approach used in this work is depicted in Algorithm 1. The main steps of the pipeline are Otsu threshold-based reflection detection, OPENCV inpainting-based reflection suppression, feature matching and tracking based image stitching and non-lambertian surface reconstruction. Feature point correspondences between frames are established using SIFT feature matching and RANSAC based pair elimination[42]. To estimate the depth map, Tsai-Shah shape from shading approach was applied. This surface reconstruction method applies a discrete approximation of the gradients and then employs the linear approximation of the reflectance function in terms of the depth directly. For further details of Tsai-Shah method, the reader is referred to the original paper [43]. Fig. 6 demonstrates the steps and output maps aligned with the ground truth scanned data. Using that pipeline, RMSEs of 1.09 cm, 1.02 cm and 1.11 cm were obtained for Colon-IV, Small Intestine and Stomach-III trajectories, respectively.

Algorithm 1 3D Reconstruction and Evaluation Pipeline

- 1: Extract SIFT features between image pairs
 - 2: Find k -nearest neighbours for each feature using a k -d tree
 - 3: **for** each image **do**
 - 4: (i) Select m candidate matching images that have the most number of corresponding feature points
 - 5: (ii) Find geometrically consistent feature matches using RANSAC to solve for the homography between pairs of images.
 - 6: **end for**
 - 7: Find connected components of image matches
 - 8: **for** each connected component **do**
 - 9: (i) Perform bundle adjustment for connected components in image matches
 - 10: (ii) Render final stitched image using multi-band blending
 - 11: **end for**
 - 12: Apply inpainting on the stitched image to suppress specularities
 - 13: Reconstruct the surface using Tsai-Shah shape from shading method
 - 14: Label a common line segment in ground truth data and reconstructed surface
 - 15: Apply ICP algorithm using the common line as initialization
 - 16: Compute iteratively the cloud-to-mesh distances to acquire RMSE
-

V. CONCLUSION

In this paper, we introduced a novel endoscopic SLAM dataset containing both capsule and standard endoscopic camera images with 6-DoF ground truth pose and high precision scanned 3D maps of explored GI organs. Four different cameras were employed in total to collect data from eight ex-vivo porcine GI-tract organs each from different animal instances. Various additional post processing effects such as fish eye distortions, blur, downsampling and vignette effects were used to variate and expand the dataset. With comprehensive quantitative tests conducted on SC-SfMLearner and a traditional 3D reconstruction pipeline, the use-case of the proposed dataset was exemplified. As a future work, we plan to benchmark and critically compare existing state-of-the-art deep SLAM algorithms using EndoSLAM dataset.

ACKNOWLEDGMENT

Mehmet Turan, Kutsev Bengisu Ozyoruk, Kagan Incetan, Guliz Irem Gokceler and Gulfiz Coskun are especially grateful to Technological Research Council of Turkey (TUBITAK) for International Fellowship for Outstanding Researchers. We would like to express deep gratitude to Abdullhamid Obeid, Hasan Sahin and Ebru Sagiroglu for their valuable support during experiments.

REFERENCES

- [1] K. Pogorelov *et al.*, “Kvasir: A multi-class image dataset for computer aided gastrointestinal disease detection,” in *Proceedings of the 8th ACM on Multimedia Systems Conference*, 06 2017.
- [2] A. Koulouzidis *et al.*, “KID Project: an internet-based digital video atlas of capsule endoscopy for research purposes,” *Endosc Int Open*, vol. 5, no. 6, pp. E477–E483, Jun 2017.
- [3] S. Moccia *et al.*, “Learning-based classification of informative laryngoscopic frames,” *Computer Methods and Programs in Biomedicine*, vol. 158, 05 2018.
- [4] V. Penza, A. S. Ciullo, S. Moccia, L. S. Mattos, and E. De Momi, “Endoabs dataset: Endoscopic abdominal stereo image dataset for benchmarking 3d stereo reconstruction algorithms,” *The International Journal of Medical Robotics and Computer Assisted Surgery*, vol. 14, no. 5, p. e1926, 2018.
- [5] American Cancer Society, *Global Cancer Facts and Figures 4th Edition*. American Cancer Society, 2018.
- [6] M. Arnold *et al.*, “Global burden of 5 major types of gastrointestinal cancer,” *Gastroenterology*, April 2020. [Online]. Available: <https://doi.org/10.1053/j.gastro.2020.02.068>
- [7] E. Redondo-Cerezo, A. Sanchez-Capilla, P. Torre-Rubio, and J. Teresa, “Wireless capsule endoscopy: Perspectives beyond gastrointestinal bleeding,” *World journal of gastroenterology : WJG*, vol. 20, pp. 15 664–15 673, 11 2014.
- [8] D. Joseph *et al.*, “Colorectal cancer screening: Estimated future colonoscopy need and current volume and capacity: Colonoscopy need and capacity,” *Cancer*, vol. 122, 05 2016.
- [9] T. Yano and H. Yamamoto, “Vascular, polypoid, and other lesions of the small bowel,” *Best practice & research. Clinical gastroenterology*, vol. 23, pp. 61–74, 02 2009.
- [10] N. Dey, A. S. Ashour, F. Shi, and R. S. Sherratt, “Wireless capsule gastrointestinal endoscopy: Direction-of-arrival estimation based localization survey,” *IEEE reviews in biomedical engineering*, vol. 10, pp. 2–11, 2017.
- [11] T. Shah, S. M. Aziz, and T. Vaithianathan, “Development of a tracking algorithm for an in-vivo rf capsule prototype,” in *2006 International Conference on Electrical and Computer Engineering*. IEEE, 2006, pp. 173–176.
- [12] D. Son, S. Yim, and M. Sitti, “A 5-d localization method for a magnetically manipulated untethered robot using a 2-d array of hall-effect sensors,” *IEEE/ASME Transactions on Mechatronics*, vol. 21, no. 2, pp. 708–716, 2015.

- [13] R. Kuth, J. Reinschke, and R. Rockelein, "Method for determining the position and orientation of an endoscopy capsule guided through an examination object by using a navigating magnetic field generated by means of a navigation device," Feb. 15 2007, uS Patent App. 11/481,935.
- [14] T. D. Than *et al.*, "An effective localization method for robotic endoscopic capsules using multiple positron emission markers," *IEEE Transactions on Robotics*, vol. 30, no. 5, pp. 1174–1186, 2014.
- [15] T. D. Than, G. Alici, H. Zhou, and W. Li, "A review of localization systems for robotic endoscopic capsules," *IEEE transactions on biomedical engineering*, vol. 59, no. 9, pp. 2387–2399, 2012.
- [16] G. Ciuti *et al.*, "Frontiers of robotic endoscopic capsules: a review," *Journal of Micro-Bio Robotics*, vol. 11, no. 1-4, pp. 1–18, 2016.
- [17] N. Simaan, R. H. Taylor, and H. Choset, "Intelligent surgical robots with situational awareness," *Mechanical Engineering*, vol. 137, no. 09, pp. S3–S6, 2015.
- [18] P. Mountney, D. Stoyanov, A. Davison, and G.-Z. Yang, "Simultaneous stereoscope localization and soft-tissue mapping for minimal invasive surgery," in *International Conference on Medical Image Computing and Computer-Assisted Intervention*. Springer, 2006, pp. 347–354.
- [19] D. Stoyanov, M. V. Scanzanella, P. Pratt, and G.-Z. Yang, "Real-time stereo reconstruction in robotically assisted minimally invasive surgery," in *International Conference on Medical Image Computing and Computer-Assisted Intervention*. Springer, 2010, pp. 275–282.
- [20] B. Lin, A. Johnson, S. Qian, J. Sanchez, and Y. Sun, "Simultaneous tracking, 3d reconstruction and deforming point detection for stereoscope guided surgery," in *Augmented Reality Environments for Medical Imaging and Computer-Assisted Interventions*. Springer, 2013, pp. 35–44.
- [21] D. J. Mirota, H. Wang, R. H. Taylor, M. Ishii, G. L. Gallia, and G. D. Hager, "A system for video-based navigation for endoscopic endonasal skull base surgery," *IEEE transactions on medical imaging*, vol. 31, no. 4, pp. 963–976, 2011.
- [22] O. G. Grasa, E. Bernal, S. Casado, I. Gil, and J. Montiel, "Visual slam for handheld monocular endoscope," *IEEE transactions on medical imaging*, vol. 33, no. 1, pp. 135–146, 2013.
- [23] R. J. Chen, T. L. Bobrow, T. L. Athey, F. Mahmood, and N. J. Durr, "Slam endoscopy enhanced by adversarial depth prediction," *ArXiv*, vol. abs/1907.00283, 2019.
- [24] M. Turan, Y. Pilavc, R. Jamiruddin, H. Araujo, E. Konukoglu, and M. Sitti. (2017, 05) A fully dense and globally consistent 3d map reconstruction approach for gi tract to enhance therapeutic relevance of the endoscopic capsule robot.
- [25] M. Turan, Y. Almalioglu, H. Araujo, E. Konukoglu, and M. Sitti, "A non-rigid map fusion-based direct slam method for endoscopic capsule robots," *International journal of intelligent robotics and applications*, vol. 1, no. 4, pp. 399–409, 2017.
- [26] M. Turan, Y. Almalioglu, H. Araújo, E. Konukoglu, and M. Sitti, "Deep endovo: A recurrent convolutional neural network (RCNN) based visual odometry approach for endoscopic capsule robots," *CoRR*, vol. abs/1708.06822, 2017. [Online]. Available: <http://arxiv.org/abs/1708.06822>
- [27] M. Turan *et al.*, "Unsupervised odometry and depth learning for endoscopic capsule robots," *arXiv preprint arXiv:1803.01047*, 2018.
- [28] H. Borgli *et al.*, "Hyper-kvasir: A comprehensive multi-class image and video dataset for gastrointestinal endoscopy," 12 2019.
- [29] J. Bernal *et al.*, "Comparative validation of polyp detection methods in video colonoscopy: Results from the miccai 2015 endoscopic vision challenge," *IEEE Transactions on Medical Imaging*, vol. 36, no. 6, pp. 1231–1249, June 2017.
- [30] S. P. Hong, J. Cheon, T. Kim, S. Song, and W. Kim, "Comparison of the diagnostic yield of "mirocam" and "pillcam sb" capsule endoscopy," *Hepato-gastroenterology*, vol. 59, pp. 778–81, 05 2012.
- [31] Artec3D. User handbook - artec3d eva. Last accessed August 2019. [Online]. Available: <https://www.artec3d.com/files/pdf/ArtecScanners-Booklet-EURO.pdf>
- [32] S. 3D. User handbook - shining 3d einscan. Last accessed August 2019. [Online]. Available: <https://www.artec3d.com/files/pdf/ArtecScanners-Booklet-EURO.pdf>
- [33] J.-W. Bian *et al.*, "Unsupervised scale-consistent depth and ego-motion learning from monocular video," 2019.
- [34] F. Mahmood and N. J. Durr, "Deep learning and conditional random fields-based depth estimation and topographical reconstruction from conventional endoscopy," *Medical Image Analysis*, vol. 48, pp. 230 – 243, 2018. [Online]. Available: <http://www.sciencedirect.com/science/article/pii/S1361841518303761>
- [35] F. Mahmood, R. Chen, and N. J. Durr, "Unsupervised reverse domain adaptation for synthetic medical images via adversarial training," *IEEE Transactions on Medical Imaging*, vol. 37, no. 12, pp. 2572–2581, 2018.
- [36] Z. Zhang, "Flexible camera calibration by viewing a plane from unknown orientations," in *Proceedings of the Seventh IEEE International Conference on Computer Vision*, vol. 1. Ieee, 1999, pp. 666–673.
- [37] R. Y. Tsai and R. K. Lenz, "A new technique for fully autonomous and efficient 3d robotics hand/eye calibration," *IEEE Transactions on Robotics and Automation*, vol. 5, no. 3, pp. 345–358, June 1989.
- [38] S. Pertuz, "Defocus simulation," *MATLAB Central File Exchange*, June 7, 2020. [Online]. Available: <https://www.mathworks.com/matlabcentral/fileexchange/55095-defocus-simulation>
- [39] [Online]. Available: <https://invesalio.github.io/>
- [40] B. K. Horn, "Closed-form solution of absolute orientation using unit quaternions," *Josa a*, vol. 4, no. 4, pp. 629–642, 1987.
- [41] A. Handa, T. Whelan, J. McDonald, and A. J. Davison, "A benchmark for rgb-d visual odometry, 3d reconstruction and slam," in *Robotics and automation (ICRA), 2014 IEEE international conference on*. IEEE, 2014, pp. 1524–1531.
- [42] M. Brown and D. G. Lowe, "Automatic panoramic image stitching using invariant features," *International Journal of Computer Vision*, vol. 74, no. 1, pp. 59–73, 2007.
- [43] T. Ping-Sing and M. Shah, "Shape from shading using linear approximation," *Image and Vision computing*, vol. 12, no. 8, pp. 487–498, 1994.
- [44] E. Spyrou and D. K. Iakovidis, "Video-based measurements for wireless capsule endoscope tracking," *Measurement Science and Technology*, vol. 25, no. 1, p. 015002, 2013.
- [45] "The Kvasir-SEG Dataset," <https://datasets.simula.no/kvasir-seg/>.
- [46] J. Bernal, J. Sanchez, and F. Vilario, "Towards automatic polyp detection with a polyp appearance model," *Pattern Recognition*, vol. 45, pp. 3166–3182, 09 2012.
- [47] J. Bernal *et al.*, "Wm-dova maps for accurate polyp highlighting in colonoscopy: Validation vs. saliency maps from physicians," *Computerized Medical Imaging and Graphics*, vol. 43, p. 99111, July 2015.
- [48] J. S. Silva, A. Histace, O. Romain, X. Dray, and B. Granado, "Towards embedded detection of polyps in WCE images for early diagnosis of colorectal cancer," *International Journal of Computer Assisted Radiology and Surgery*, vol. 9, no. 2, pp. 283–293, 2014.
- [49] N. Tajbakhsh, S. R. Gurudu, and J. Liang, "Automated polyp detection in colonoscopy videos using shape and context information," *IEEE Transactions on Medical Imaging*, vol. 35, no. 2, pp. 630–644, Feb 2016.
- [50] M. Ye, S. Giannarou, A. Meining, and G.-Z. Yang, "Online tracking and retargeting with applications to optical biopsy in gastrointestinal endoscopic examinations," *Medical image analysis*, vol. 30, pp. 144–157, 2016.
- [51] M. Ye, E. Johns, A. Handa, L. Zhang, P. Pratt, and G.-Z. Yang, "Self-supervised siamese learning on stereo image pairs for depth estimation in robotic surgery," *arXiv preprint arXiv:1705.08260*, 2017.
- [52] "Robust medical instrument segmentation (robust-mis) challenge 2019," <https://www.synapse.org/#!/Synapse:syn18779624/wiki/592660>, accessed: 2020-02-12.
- [53] D. Honegger, P. Greisen, L. Meier, P. Tanskanen, and M. Pollefeys, "Real-time velocity estimation based on optical flow and disparity matching," in *2012 IEEE/RSJ International Conference on Intelligent Robots and Systems*. IEEE, 2012, pp. 5177–5182.
- [54] H. W. Ho, G. C. de Croon, and Q. Chu, "Distance and velocity estimation using optical flow from a monocular camera," *International Journal of Micro Air Vehicles*, vol. 9, no. 3, pp. 198–208, 2017.
- [55] C. McCarthy, N. Barnes, and R. Mahony, "A robust docking strategy for a mobile robot using flow field divergence," *IEEE Transactions on Robotics*, vol. 24, no. 4, pp. 832–842, 2008.
- [56] B. D. Lucas and T. Kanade, "An iterative image registration technique with an application to stereo vision," *Proceedings of the 7th international joint conference on Artificial intelligence*, 1981.
- [57] G. Liu, "On velocity estimation using position measurements," in *Proceedings of the 2002 American Control Conference (IEEE Cat. No. CH37301)*, vol. 2. IEEE, 2002, pp. 1115–1120.
- [58] L. J. Puglisi, "On the velocity and acceleration estimation from discrete time-position signal of linear encoders," *Journal of Control Engineering and Applied Informatics*, vol. 17, no. 3, pp. 30–40, 2015.

APPENDIX A. EQUIPMENT

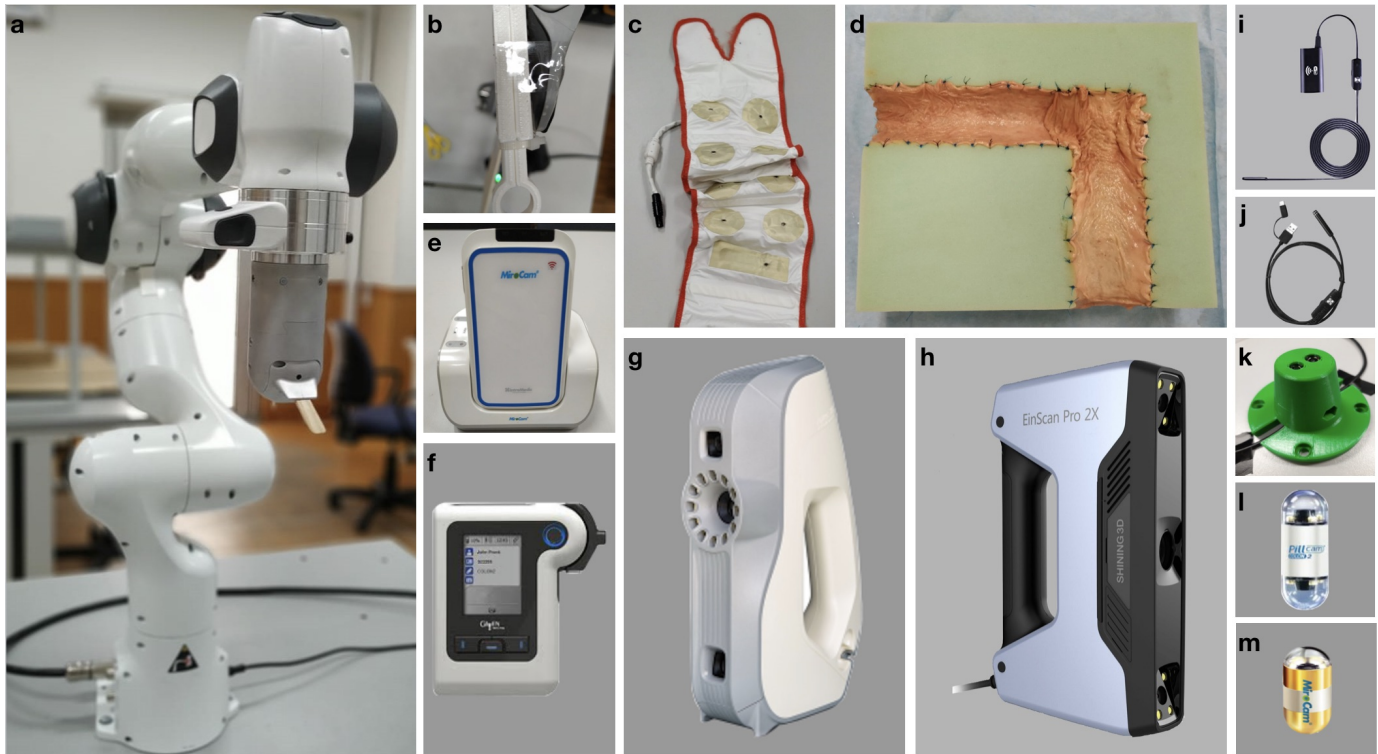


Fig. 7: **Equipment.** The equipment employed during generation of the dataset. **a** Franka Emika Panda: robotic arm employed as motion device. **b** Capsule Holder: special production two-piece holder used as a medium between the WCE cameras and the robotic arm. **c** MiroCam[®] Data Belt PillCam[®] capsule endoscope **d** Real Porcine Colon: sewn onto an 'L' shaped semi-cylindrical scaffold in high-density foam. **e** MiroCam[®] MR1100 receiver: Digital video grabber that converts analog data from receiver into digital to computer. **f** PillCam[®] recorder **g** Artec Eva: 3D scanner used to generate ground truth - ply file. **h** EinScan Pro 2X: 3D scanner used to generate ground truth - .ply, .obj, .stl and .ASC file. **i** Wireless Endoscope Camera (YPC-HD720P): high resolution - 1280720 and HD640480. **j** Endoscope 3 in 1 Camera: low resolution - 640480. **k** Camera Holder: special design one-piece holder for the high and low resolution endoscope cameras used to fixed on the robotic arm. **l** PillCam[™] COLON2: WCE double tip camera. **m** MiroCam[®] Regular MC1000-W: WCE camera employed to record frames from real porcine stomach and send to receiver.

APPENDIX B. SURVEY OF EXISTING DATASET

Related to survey section the details of the existing datasets in terms of image and video sizes, segmentation, disease classification and the detected technology of the capsule endoscopy are presented.

- The KID Dataset is organized by The Medical Decision Support Systems (MDSS) research group of the University of Thessaly. The dataset is divided into two annotated sections. The first section has a total of 77 wireless capsule endoscopy (WCE) images acquired using MiroCam® (IntroMedic Co, Seoul, Korea) capsules and has some types of abnormalities such as angioectasias, apthae, chylous cysts and polypoid lesions. The second part consists of 2,371 MiroCam® WCE. This dataset not only includes small bowel lesions such as polypoid, vascular and inflammatory lesions but also images from healthy esophagus, stomach, small bowel and colon [2]. Given Imaging Atlas Dataset consists of 20 second video clips recorded using PillCam capsules with a resolution of 576x576 pixels. In this database, 117 WCE video clips have been acquired from the small bowel, 5 from esophagus and 13 from the colon [44].
- The Kvasir dataset was collected via standard endoscopic equipments at Vestre Viken (VV) Health Trust in Norway. The initial dataset consists of 4,000 images with eight classes namely Z-line, pylorus, cecum, esophagitis, polyps, ulcerative colitis, dyed and lifted polyps and dyed resection margins of images, each represented with 500 images. All images are annotated and verified by experienced endoscopists [1]. Later, the dataset extended to 8,000 images with the same eight classes [28]. The Kvasir-SEG Dataset is an extension of the Kvasir dataset which is used for polyp segmentation. It comprises 1000 polyp images and their corresponding ground truth from the second version of the Kvasir dataset [45].
- The Hyper-Kvasir dataset is the largest online available dataset related to the gastrointestinal tract, containing 110,079 images (10,662 labeled and 99,417 unlabeled images) and 373 videos, making a total of 1.17 million frames. The entire dataset was collected in gastro- and colonoscopy examinations in Norway and 10,662 images are labeled for 23 classes by practitioners. [28].
- The NBI-InfFrames dataset includes Narrow-band imaging(NBI) endoscopy which is commonly used as a diagnostic procedure to examine the back of throat, glottis, vocal cords and the larynx. To generate this in vivo dataset, 18 different patients affected by laryngeal spinocellular carcinoma (diagnosed after histopathological examination) were involved. It consists of 180 informative (I), 180 blurred (B), 180 with saliva or specular reflections (S) and 180 underexposed (U) frames with a total number of 720 video frames [3].
- The EndoAbS(Endoscopic Abdominal Stereo Images) Dataset consists of 120 sub-datasets of endoscopic stereo images of abdominal organs (e.g., liver, kidney, spleen) with corresponding ground truth acquired via laser scanner. In order to create variations in the dataset, frames have been recorded under 3 different lighting conditions, presence of smoke and 2 different distances from endoscope to phantom (~ 5 cm and ~ 10 cm). The main purpose of generating this dataset was to validate 3D reconstruction algorithms for the computer assisted surgery community [4].
- CVC-ColonDB is a database of annotated video sequences consisting of 15 short colonoscopy sequences, where one polyp has been shown in each sequence. There are 1,200 different images containing original images, polyp masks, non-informative image masks and contour of polyp masks. It can be used for assessment of polyp detection [46].
- MICCAI 2015 Endoscopic Vision Challenge [29] provides three sub-databases which are CVC-ClinicDB, ETIS-Larib and ASU-Mayo Clinic polyp database and which can be used for polyp detection and localization. CVC-ClinicDB is a cooperative work of the Hospital Clinic and the Computer Vision Center, Barcelona, Spain. It contains 612 images from 29 different sequences. Each image has its annotated ground truth associated, covering the polyp [47]. ETIS-Larib is a database consisting of 196 frames of polyps extracted from colonoscopy videos. Frames and their ground truths are provided by ETIS laboratory, ENSEA, University of Cergy-Pontoise, France [48]. The ASU-Mayo Clinic polyp database was acquired as a cooperative work of Arizona State University and Mayo Clinic, USA. It consists of 20 short colonoscopy videos (18,902 frames) with different resolution ranges and different area coverage values for training purposes. Each frame in its training dataset comes with a ground truth image or a binary mask that indicates the polyp region. In addition, it contains 18 videos without annotation for testing purposes [49].
- The Hamlyn Centre Laparoscopic/Endoscopic Video Dataset consists of 37 subsets. The Gastrointestinal Endoscopic Dataset includes 10 videos and consists of 7,894 images with a size of 2.5 GB which were collected during standard gastrointestinal examinations. The dataset includes images for polyp detection, localization and optical biopsy retargeting. Apart from endoscopy dataset for depth estimation, one of the laparoscopy datasets contains 40,000 pairs of rectified stereo images collected in partial nephrectomy using Da Vinci surgery robot. Its primary use has been training and testing deep learning networks for disparity (inverse depth) estimation [50], [51].
- ROBUST-MIS Challenge provides a dataset which was created in the Heidelberg University Hospital, Germany during rectal resection and proctocolectomy surgeries. Videos from 30 minimal invasive surgical procedures with three different types of surgery and extracted 10,040 standard endoscopic image frames from these 30 procedures performed a basis for this challenge. These images were acquired using a laparoscopic camera (Karl Storz Image 1) with a 30° optic and a resolution of 1920x1080 pixels. The images are, then, downscaled to 960x540 pixels and annotated with numbers showing the absence or presence of medical instruments [52].

APPENDIX C. CAMERA CALIBRATION

For the coordinate transformation between robot pose data and capsule cameras, hand-eye calibration procedure was repeated with two different checkerboards: one with 2×2 mm squares and one with 1.5×1.5 mm squares, both patterns with 8×7 squares in total. Four images of each checkerboard were acquired from different camera poses. For the pose conversions, only the checkerboard images from Mirocam capsule was used, with the support structure being the same for both capsules (Pillcam and Mirocam). Similarly, to calculate the transformation between the gripper holding HighCam-LowCam and the camera positions, same procedure is repeated by using the checkerboard squares with 10.2×10.2 mm.

The Tsai and Lenz algorithm[37] was tested with 24 combinations of the 4 chessboard images in Fig. 8. The transformation between a point \mathbf{X}_c in the reference frame of the camera and a point \mathbf{X}_g in the reference frame of the gripper is, thus, given by

$$\mathbf{X}_g = \mathbf{R}_g^c \mathbf{X}_c + \mathbf{t}_g^c \quad (4)$$

with the rotation matrices and translation vectors given in Table IV.

TABLE IV: **Robot Pose to Camera Transformation.** The rotation matrices and translation vectors required to apply transformation given in Eqn. 4. These values are provided as a .txt file and as a .mat file in the calibration folders.

Camera	Rotation \mathbf{R}_g^c	Translation \mathbf{t}_g^c (mm)
MiroCam	$\begin{bmatrix} -0.9366 & -0.3242 & -0.1325 \\ 0.1738 & -0.1017 & -0.9795 \\ 0.3041 & -0.9405 & 0.1516 \end{bmatrix}$	$\begin{bmatrix} 2.9793 \\ -27.0224 \\ 72.1070 \end{bmatrix}$
HighCam	$\begin{bmatrix} 0.9463 & -0.0921 & -0.3098 \\ -0.1389 & 0.7495 & -0.6472 \\ 0.2918 & -0.6555 & 0.8965 \end{bmatrix}$	$\begin{bmatrix} -46.2017 \\ 20.9074 \\ 94.6349 \end{bmatrix}$
LowCam	$\begin{bmatrix} 0.8294 & 0.5577 & 0.0322 \\ -0.5586 & 0.8286 & 0.0379 \\ -0.0056 & -0.0495 & 0.9988 \end{bmatrix}$	$\begin{bmatrix} 6.0169 \\ 39.5114 \\ 101.6431 \end{bmatrix}$

For the detailed description of vision based calibration technique and its written codes in MATLAB R2020a, visit <https://github.com/CapsuleEndoscope/EndoSLAM>. Calibration was performed for both the Mirocam and Pillcam capsules, using images of a planar checkerboard with 8×7 squares of dimension 2×2 mm and also for HighCam and LowCam using 8×7 squares of dimension 12.8×12.8 mm. The calibration checkerboard was printed using a laser printer and then glued on the surface of a glass plate to ensure the planarity of the pattern.

The practical distance and orientation range at which the calibration checkerboard can be placed is limited by the low resolution and depth of field of the cameras. For each camera, 10 calibration images were used with the pattern placed at different poses. The average distance from the camera was approximately 10 mm for capsule cameras. Fig. 8 show examples of some of the calibration images.

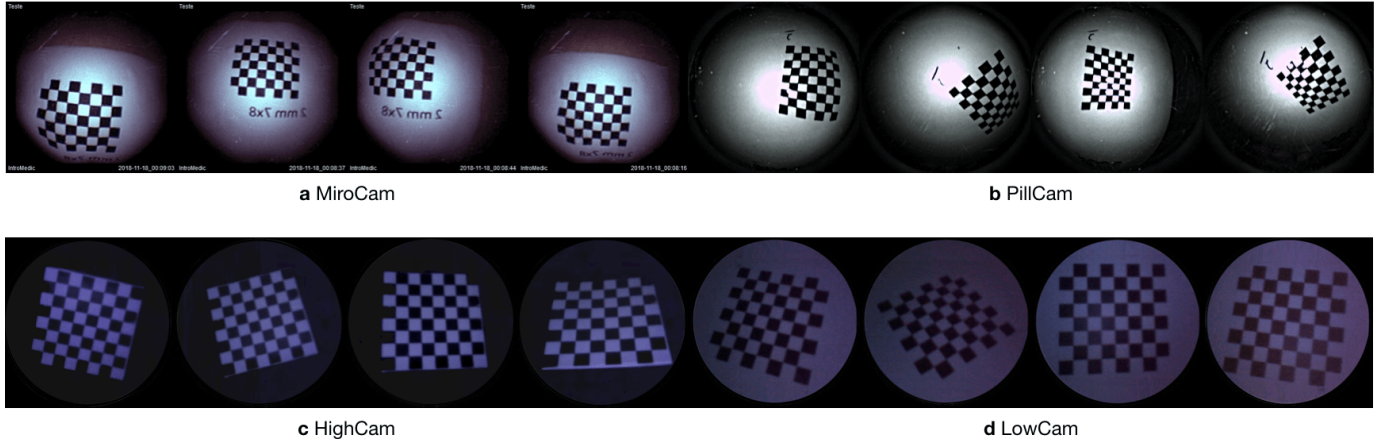


Fig. 8: **Camera Intrinsic-Extrinsic Calibration Images.** Examples of planar checkerboard calibration images obtained by **a** MiroCam, **b** PillCam, **c** HighCam and **d** LowCam. The chessboards were printed with a laser printer and then glued on the surface of a planar glass to ensure the planarity of the pattern. Since the dataset is recorded in dark room to mimic the human GI tract, chessboard images are also taken under same environmental conditions.

Table V summarizes the estimated intrinsic parameters for each of the calibration models. Note that the Pillcam capsule has both a front-facing and a backwards-facing camera. That dual camera setup can lead to interesting novel visual SLAM approaches that makes simultaneous use of front- and backwards-facing cameras. The reprojection errors associated with each calibration can be seen in Fig. 9. Fig. ?? shows some examples for the application of estimated intrinsic parameters to correct the lens distortion effects on capsule images to produce undistorted pinhole images. Note that eight images were used due to the limited operational volume to place the chessboard. Outside that volume the images become either less focused/blurry or if too far the corners are undetectable due to low image quality and resolution.

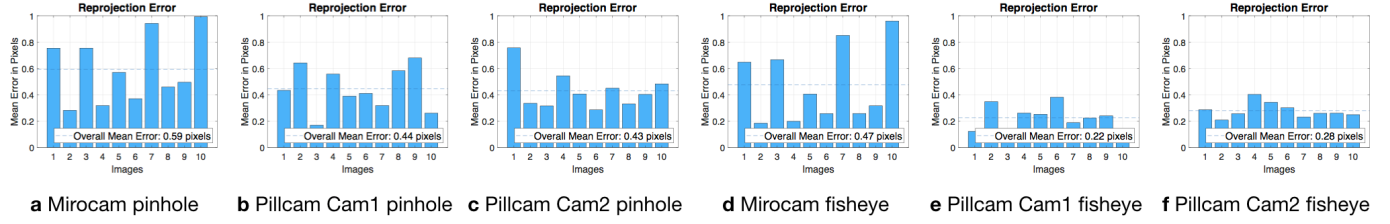


Fig. 9: **Reprojection errors associated with the camera calibrations.** Note that Pillcam has a front-facing (Cam1) and a backwards-facing (Cam2) camera. Fig. a-c show the reprojection errors using the pinhole model, while Fig. d-f show the reprojection errors using the fisheye model.



Fig. 10: **Correction of lens distortions.** Examples to correct the lens distortions via camera parameters given in Table V for the images acquired by PillCam and MiroCam. **a** Original 8×7 checkerboard image with 2×2 mm squares obtained by PillCam, **b** Undistorted checkerboard image with pinhole calibration parameters, **c** Undistorted checkerboard image with fisheye parameters, **d** Newspaper image which is rich in texture details taken by Front camera of PillCam **e** Undistorted counterpart of newspaper image with the calculated parameters under fisheye camera assumption. Similarly, **f** original Colon-III image of MiroCam and **g** undistorted version by the parameters of fisheye calibration model

TABLE V: **Intrinsic parameters for MiroCam, PillCam, HighCam and LowCam under the pinhole assumption** Since the effects mentioned in Sec. III-B are directly related with camera lens properties, the intrinsic parameters representing new images are also changing compatible with modifications. For the mixture of Gaussian blur, vignetting and resizing effects, the new parameters are given in High-Modified and Low-Modified columns.

							PillCam		
							Cam1	Cam2	
Image size (pix)			480×640	480×640	400×400	250×250	320×320	256×256	256×256
Pinhole	Focal length	f_x	957.4119	816.8598	603.5105	317.6319	156.0418	74.2002	76.0535
		f_y	959.3861	814.8223	807.6887	423.1068	155.7529	74.4184	75.4967
	Skew	s	5.6242	0.2072	4.2831	-0.3334	0	0	0
	Optical center	c_x	282.1921	308.2864	173.7160	121.3764	178.5604	129.9724	130.9419
		c_y	170.7316	158.3971	133.7022	82.5754	181.8043	129.1209	128.4882
	Radial dist. coef.	k_1	0.2533	0.2345	0.2645	0.2265	-0.2486	0.1994	0.1985
		k_2	-0.2085	-0.7908	-0.4186	-0.8877	0.0614	-0.1279	-0.1317

APPENDIX D. TEMPORAL-SYNCHRONIZATION

The apparent velocity field in the image, i.e. the optical flow, is the projection of the 3D velocity of the scene (w.r.t. the camera), and is, in general, dependent on scene depth [53]. In the dataset, the camera moves, roughly, in a straight line along its optical axis and with limited rotation, for the most part of the trajectory. The scene is also relatively uniform and symmetric, in terms of relative depth. To estimate this "forward" motion, the divergence of the flow vector field can be used [54], [55]. To provide insight, Fig. 11a shows the divergent optical flow field that would be obtain as a pinhole camera moves towards a frontal-parallel plane. Fig. 11b shows an example, obtained from the dataset, of divergent optical flow in image areas of high contrast.

The divergence at an image point (x, y) is given by

$$D(x, y) = \frac{\partial u(x, y)}{\partial x} + \frac{\partial v(x, y)}{\partial y} \quad (5)$$

where u and v are the velocity components of the optical flow field and ∂ denotes a partial derivative. The divergence measurement is averaged across all points, yielding a single estimated value for each image. MATLAB was used to compute the optical flow and the flow divergence, using the method in [56].

The robot encoder data provides the camera pose along the trajectory. The linear velocity is computed by applying a finite difference on the position data, followed by a low pass filter [57], [58]. Specifically, the camera velocity v is obtained from

$$v_k = \left\| \frac{\mathbf{X}_k - \mathbf{X}_{k-1}}{T} \right\| \quad (6)$$

where \mathbf{X} denotes the 3D position vector, T denotes the sampling period, and the subscript k indexes the sample instant. A low pass Butterworth filter (with a cutoff frequency of 300Hz) is then applied to the velocity measurement in order to reduce noise.

The optical flow divergence and camera velocity measurements are correlated along the time axis to determine the best alignment. As an example, Fig. 11c shows the camera velocity (magnitude) during sequence/experiment for the sixth sequence of MiroCam record, calculated from the robot position data and estimated from the divergence of the optical flow field in the images. Both signals are shown already synchronized. Fig. 11d shows a detail of the plot corresponding to the end of the trajectory, when the camera stops moving.

Table VI and VII summarize the temporal synchronization for all trajectories in the dataset. They provide a correspondence between the start frame of each sequence and the matching sampling instant of the robot pose data.

TABLE VI: **Temporal synchronization.** Correspondence, for each sequence of each organ, between the first frame of the trajectory for both HighCam and LowCam and the matching sample instant of the robot data with 1kHz recording frequency.

Organ	Trajectory	Camera		Robot	
		HighCam Start Frame	LowCam Start Frame	HighCam Sample	LowCam Sample
Colon-IV	1	741	393	35,295	15,845
	2	44	128	2,561	2,561
	3	69	82	3,975	3,975
	4	138	120	15,792	15,092
	5	99	144	1,270	3,270
Small Intestine	1	149	95	5,162	4,512
	2	133	112	4,913	2,763
	3	186	144	6,095	7,845
	4	121	79	3,205	3,205
	5	138	105	3,807	3,307
Stomach - I	1	60	135	4,443	8,093
	2	111	144	4,177	2,277
	3	71	447	6,058	19,008
	4	47	316	2,839	13,289
Stomach - II	1	255	125	9,641	5,141
	2	1	2	3,358	3,358
	3	150	83	5,797	2,247
	4	78	85	2,742	4,192
Stomach - III	1	195	89	6,746	2,846
	2	302	108	1,523	2,725
	3	387	105	17,261	2,861
	4	125	60	4,451	2,101

TABLE VII: **Temporal synchronization.** Correspondence, for each sequence, between the first frame of the trajectory and the matching sample instant (sample number) of the robot data. Note that, in the Pillcam capsule, Cam1 (front facing camera) and Cam2 (backward facing camera) trigger alternatively, one after the other, with equally spaced time intervals. The values indicated in the table correspond to Cam1.

Sequence	Camera		Robot		
	start frame	framerate	sample instant	sampl. freq.	
Mirocam	1	336	3 fps	72,050	1kHz
	2	153	3 fps	961	1kHz
	3	321	3 fps	47,667	1kHz
	4	143	3 fps	33,943	1kHz
	5	254	3 fps	2,886	1kHz
	6	134	3 fps	3,044	1kHz
Pillcam	"L"	1,127	0.117 fps	15,800	1kHz
	"Z"	815	0.117 fps	11,650	1kHz

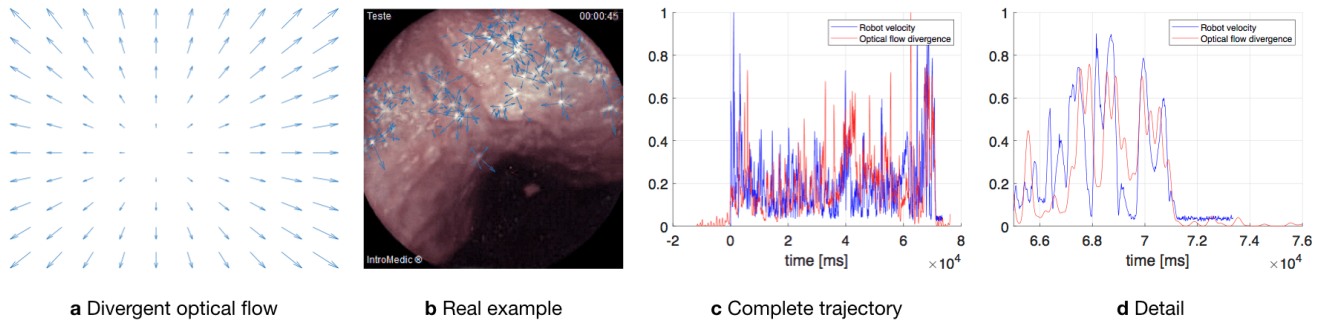


Fig. 11: **Optical flow and temporal synchronization of robot data and images.** The Divergence of the optical flow field is used to estimate the forward motion of the camera. Fig. **a** shows the divergent optical flow field obtained as a pinhole camera moves towards a frontal-parallel plane. Fig. **b** shows an example, obtained from the dataset, of divergent optical flow detected in image areas of high contrast. Fig. **c** shows the camera velocity (magnitude) during sequence/experiment *seq6 Mirocam*, obtained from the robot position data (low pass filter was used to reduce noise), and estimated from the divergence of the optical flow field in the images (see main text for details). The vertical scale is normalized for both measurements. The signals are correlated and aligned to obtain temporal synchronization. Fig. **d** shows a detail of the plot corresponding to the end of the trajectory, when the camera comes to a stop.

APPENDIX E. DATA TREE STRUCTURE

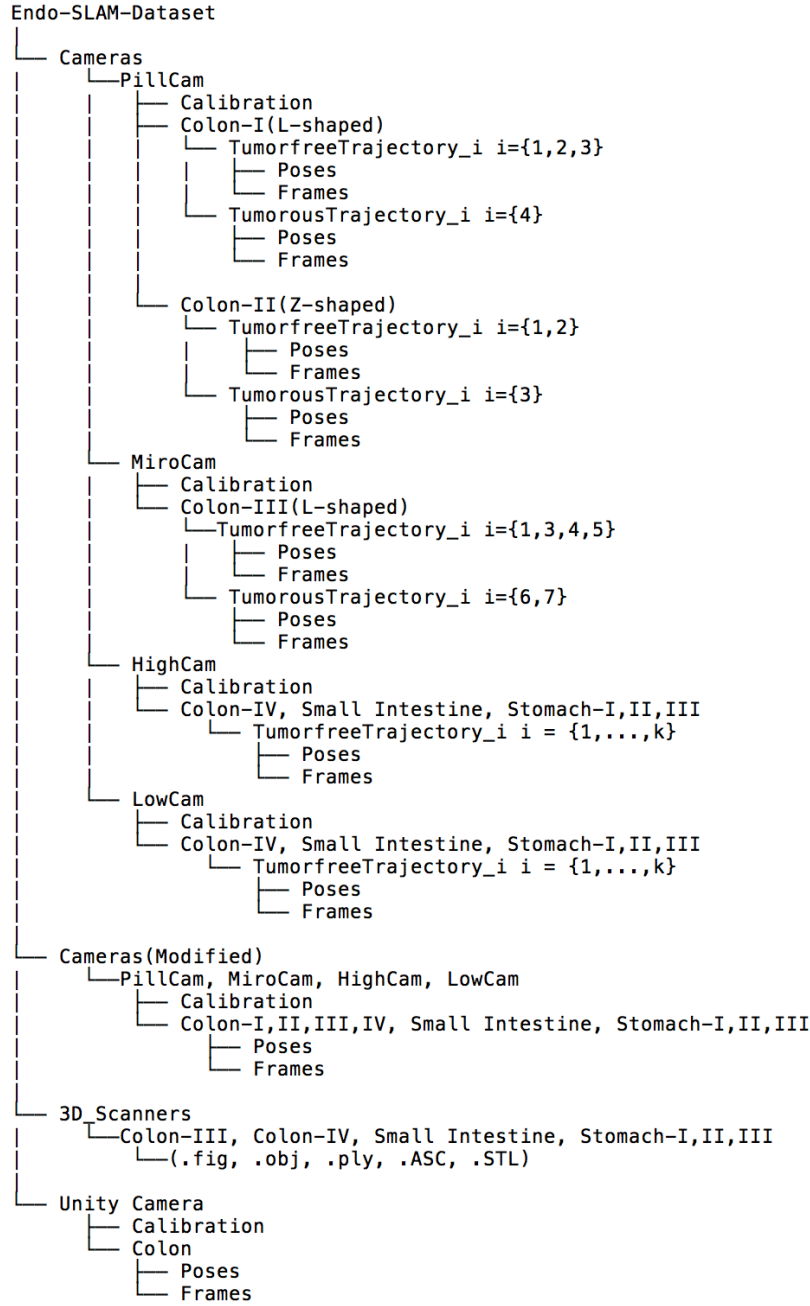


Fig. 12: **Data Tree.** The EndoSLAM dataset is divided into four main parts: Cameras, Cameras (Modified), 3D_Scanner and Unity Camera. Cameras and Cameras (Modified) folders include four subfolders as PillCam, MiroCam, HighCam and LowCam. Each of them branch out into calibration and organs subfolders. Calibration subfolder comprises intrinsic-extrinsic camera parameters and corresponding calibration sessions whereas organs subfolder includes images and poses of each trajectories. Apart from Cameras section, modified part includes sample sub-trajectories exemplifying the effects of image modification functions such as fish-eye, Gaussian blur, vignetting, resizing, depth of fields. 3D_Scanner folder consists of reconstructed 3D figures (.fig), point cloud data (.ply), surface geometry of three-dimensional objects without any color or texture representations (.STL), the position of each vertex representing 3D geometry(.obj) and ASCII formatted point cloud data(.ASC). and finally Unity Camera folder includes synthetically generated images and corresponding poses.

APPENDIX F. DATASET ANALYSIS

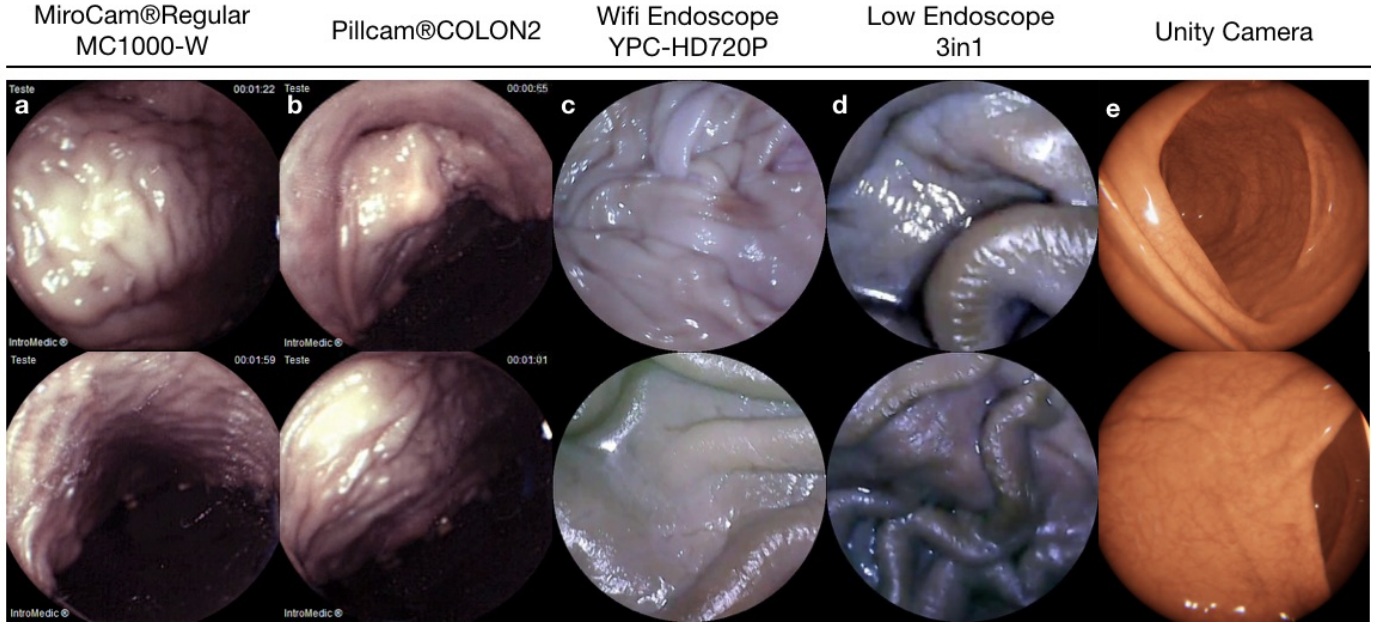


Fig. 13: **Collection of frames taken on endoscope trajectories.** **a** was collected by MiroCam **b** was acquired by the frontal camera of a PillCam **c** was acquired by the HighCam **d** was acquired by the LowCam **e** is synthetically generated data using Unity, real patient CT images and textures rigged from real capsule endoscope videos.

TABLE VIII: **Motion Analysis.** Statistics for robot poses matching with frames of HighCam. For all trajectories of each organ, counts of robot sample instances, mean, first quantile(1st QT), median, third quantile(3rd QT), minimum, maximum speed[mm/s] values are given.

		Stomach-I	Stomach-II	Stomach-III	Small Intestine	Colon-IV
Speed	count	4695	3302	3230	6487	3697
	mean[mm/s]	18.256	19.471	20.031	16.764	17.123
	std[mm/s]	22.497	16.809	16.697	14.210	12.660
	1st QT	5.931	7.606	7.055	5.684	7.658
	median	14.642	16.021	16.489	13.849	15.096
	3rd QT	25.32	26.64	28.68	24.342	24.324
	min[mm/s]	0.02	0.028	0.02	0	0.007
	max[mm/s]	25.32	140.898	116.984	104.08	104.759
Acceleration	mean[mm/s]	359.843	382.928	383.829	328.568	326.241
	std	450.939	337.08	336.098	284.423	257.08
	1st QT	110.408	140.982	111.71	103.129	122.807
	median	284.729	314.784	315.012	269.316	283.728
	3rd QT	501.31	528.799	556.451	477.991	469.113
	min[mm/s]	0.4	0.0	0.0	0.0	0.015
	max[mm/s]	14,680.15	2,817.962	2,339.683	2,079.994	2,095.182

TABLE IX: **Motion Analysis.** Statistics for robot poses matching with frames of LowCam. For all trajectories of each organ, counts of robot sample instances, mean, first quantile(1st QT), median, third quantile(3rd QT), minimum, maximum speed[mm/s] values are given.

		Stomach-I	Stomach-II	Stomach-III	Small Intestine	Colon-IV
Speed	count	2302	2799	3900	5098	3857
	mean[mm/s]	15.599	18.928	25.97	17.918	17.144
	std[mm/s]	12.855	14.431	21.564	14.764	12.882
	1st QT	5.407	8.259	10.789	6.126	7.401
	median	13.18	15.871	21.284	15.322	15.148
	3rd QT	22.956	26.436	35.763	26.146	24.455
	min[mm/s]	0.02	0.0	0.02	0.0	0.028
	max[mm/s]	79.042	103.254	286.68	97.315	106.271
Acceleration	mean[mm/s]	279.254	378.346	519.361	334.373	355.941
	std	253.777	288.769	431.327	295.646	259.482
	1st QT	66.573	164.972	215.786	119.299	130.256
	median	221.297	317.344	425.678	303.582	291.994
	3rd QT	428.253	528.695	715.263	520.839	482.864
	min[mm/s]	0.4	0.0	0.0	0.0	0.015
	max[mm/s]	1,580.846	2,065,071	5,733.593	1,946.305	2,125.42

TABLE X: **The Classification of Trajectories** The recorded trajectories for each organ divided into two groups based on the tumorous properties of tissue as tumor-containing and tumor-free. Approximately 10% of all trajectories is tumorous which might be practical for segmentation and disease classification tasks.

Organs	Tumor-free Trajectory #	Tumor-containing Trajectory #
Colon-I	I,II,III,	IV
Colon-II	I,III,IV,V	VI,VII
Colon-III	I,II	III
Colon-IV	I,II,III,IV,V	-
Stomach-I	I,II,III,IV	-
Stomach-II	I,II,III,IV	-
Stomach-III	I,II,III,IV	-
Small Intestine	I,II,III,IV,V	-

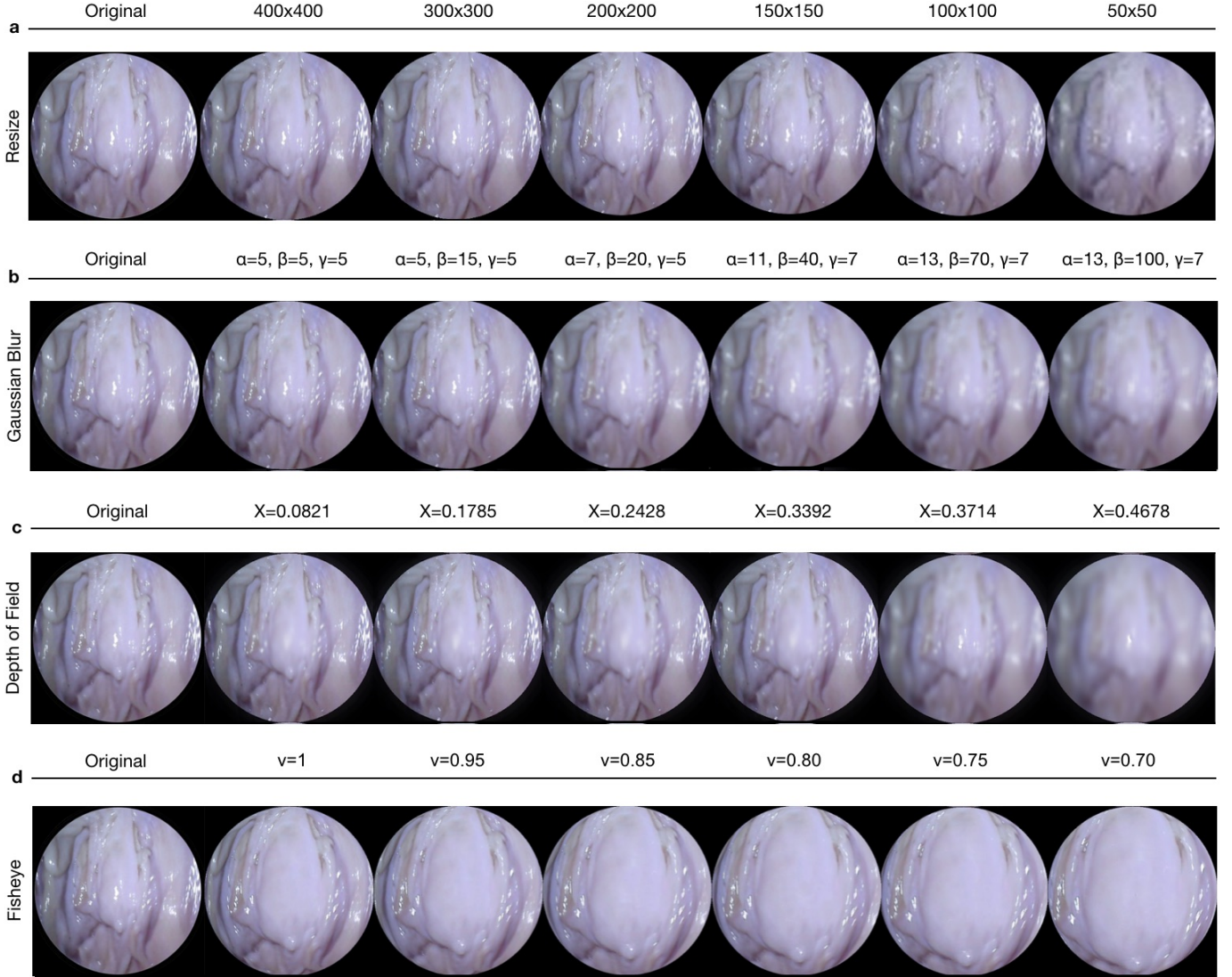


Fig. 14: **Image Modifications.** **a Resize** The size of the images, width \times height, from left to right is given as 400 \times 400, 300 \times 300, 200 \times 200, 150 \times 150, 100 \times 100 and 50 \times 50, **b Gaussian Blur** with convolution filter size(α) are 5 \times 5, 5 \times 5, 7 \times 7, 11 \times 11, 13 \times 13 and 13 \times 13 and standard deviation of Gaussian distribution(β) 5, 15, 20, 40, 70, 100 and the number of filtering times(γ) 5, 5, 5, 7, 7, 7. **c Depth of Field** effects for the focus positions 0.0821, 0.1785, 0.2428, 0.3392, 0.3714, 0.4678, **d Fish Eye** distortion for discarding ratios ν for 1, 0.95, 0.85, 0.8, 0.75, 0.7.

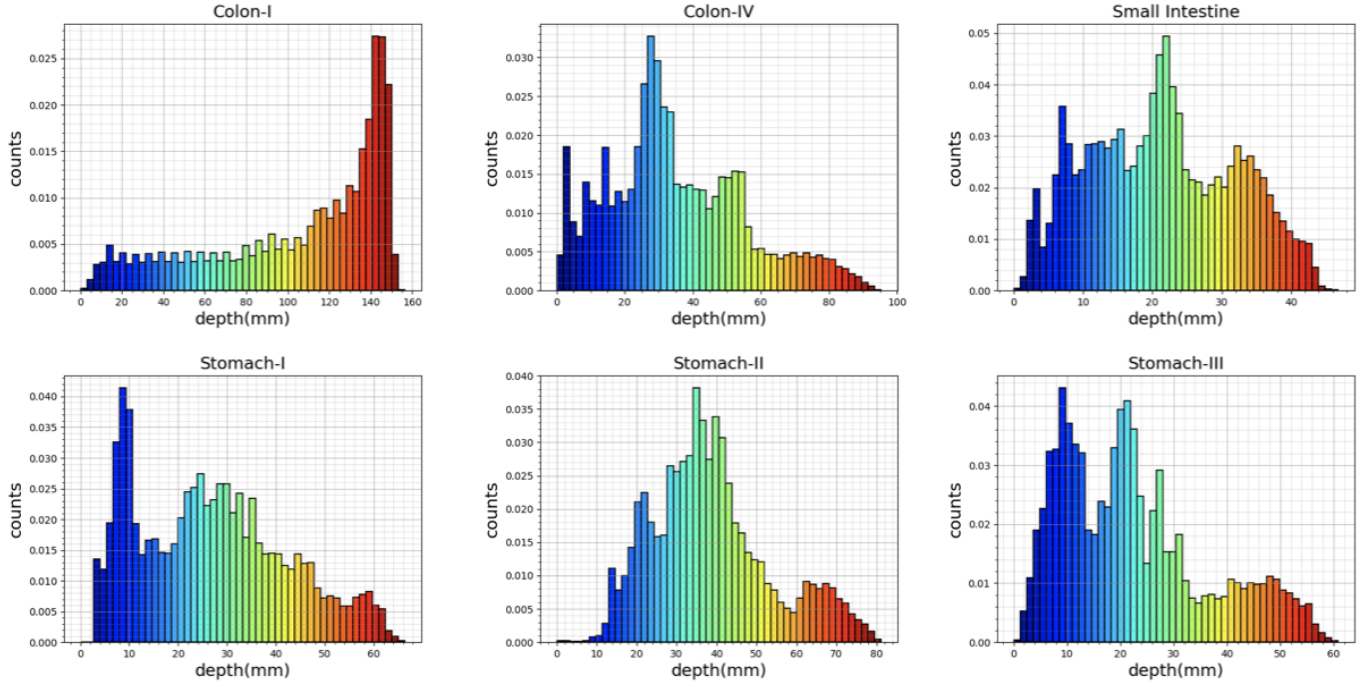


Fig. 15: **Depth Evaluation of Point Cloud Data.** The frequency distribution of depth values of **a** Colon-I which is used to collect data by Mirocam, **b** Colon-IV in the second part of the dataset, **c** Small-Intestine, **d-f** are stomachs z measured in mm.

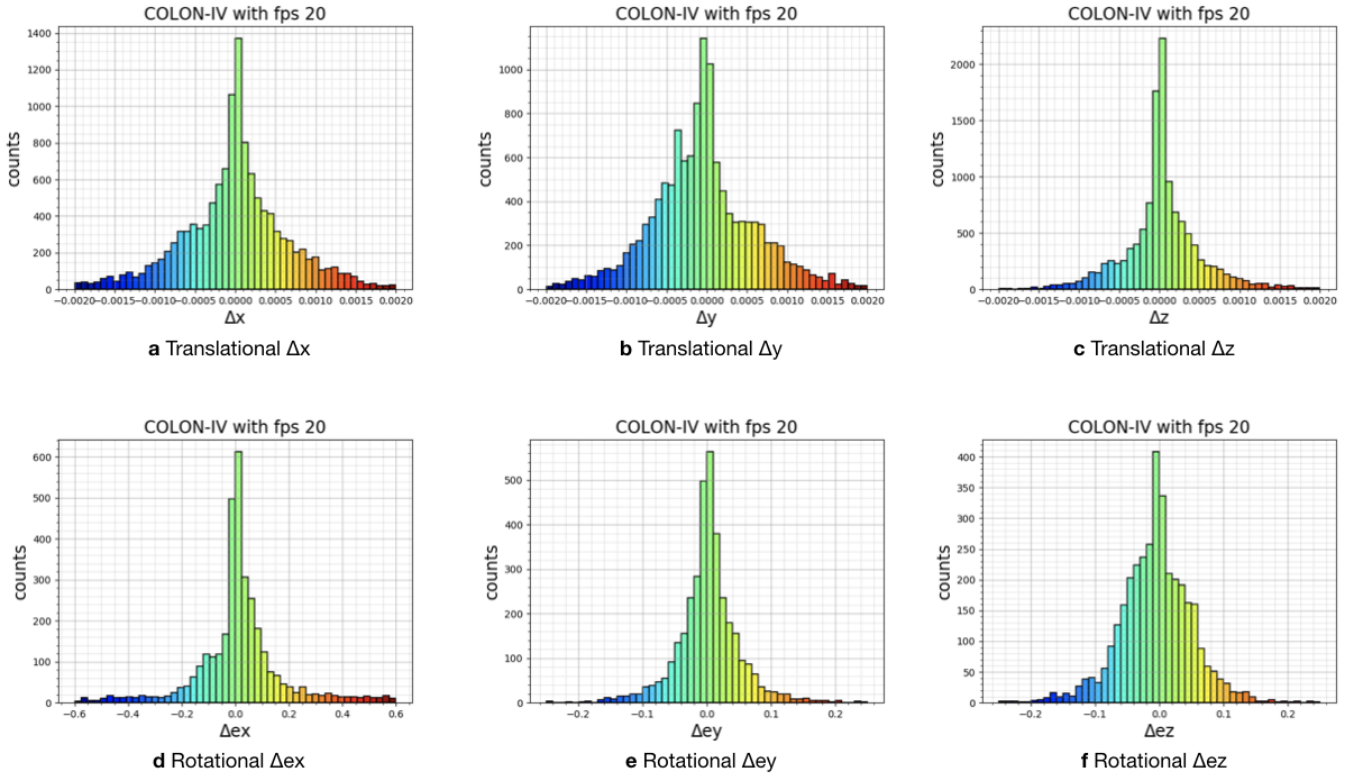


Fig. 16: **Motion Analysis Histograms** The frequency distribution of positional differences between two consecutive frames along the **a** x , **b** y , **c** z axis and the rotational differences in **d** x , **e** y , **f** z axis in terms of Euler angles are given.

APPENDIX G. RESULTS

TABLE XI: **Quantitative results of pose prediction for various organs and trajectories.** Unsupervised pose estimation algorithm SC-SfMLearner [33] is evaluated using Absolute Trajectory Error (ATE), Translational and Rotational Relative Pose Error (RPE) metrics. The results are listed for three different organs and six different trajectories using a HighCam modified versions(HighModified) with added effects (Gaussian blur with parameters $\alpha=5$, $\beta=1$, $\gamma=5$ applied after resizing images of the HighCam as 400×400 and LowCam blurred with the same parameters after resizing as 250×250 to obtain the results in LowModified). Higher ATE scores and rotational errors for the trajectories on which the excessive robot movement caused blur (e.g., Stomach-III trajectories) show that the performance of SC-SfMLearner decreases in predicting the robot position once motion blur caused by fast frame-to-frame motions occurs.

Organ, Trajectory		Trajectory Length [m]	ATE (mean \pm std) [m]	Trans. RPE (mean \pm std) [m]	Rot. RPE (mean \pm std) [deg]	Trajectory Length [m]	ATE (mean \pm std) [m]	Trans RPE (mean \pm std) [m]	Rot RPE (mean \pm std) [deg]
Model-I	HighModified					LowModified			
	Colon-IV,Traj-I	0.4286	0.5621 \pm 0.5334	0.1778 \pm 0.0698	11.6494 \pm 3.5108	0.6785	0.1862 \pm 0.1439	0.1492 \pm 0.0581	10.0931 \pm 2.2472
	Colon-IV,Traj-V	1.2547	0.3774 \pm 0.2466	0.0827 \pm 0.0977	5.3418 \pm 4.6402	1.1699	0.3542 \pm 0.286	0.0674 \pm 0.1022	4.4233 \pm 3.4051
	Intestine,Traj-I	1.2028	1.9686 \pm 2.0697	0.3162 \pm 0.3343	10.7727 \pm 3.745	0.8460	0.9796 \pm 0.7207	0.2718 \pm 0.3308	9.4257 \pm 2.2797
	Intestine,Traj-IV	1.0557	1.0886 \pm 0.9122	0.0983 \pm 0.1628	5.1528 \pm 5.1754	0.8265	0.2958 \pm 0.2475	0.0959 \pm 0.1493	4.6637 \pm 3.3413
	Stomach-III,Traj-I	1.1392	0.5174 \pm 0.5007	0.1034 \pm 0.2127	4.2815 \pm 4.2571	1.1621	1.5622 \pm 1.2892	0.2512 \pm 0.2437	8.4864 \pm 2.3824
Model-II	Stomach-III,Traj-II	1.2948	0.6443 \pm 0.5223	0.1336 \pm 0.2735	4.8712 \pm 4.7619	1.3883	1.7412 \pm 1.2662	0.2917 \pm 0.2399	9.2386 \pm 3.0266
	Colon-IV,Traj-I	0.4286	0.0835 \pm 0.0675	0.0126 \pm 0.005	1.2821 \pm 0.4742	0.6785	0.1253 \pm 0.0984	0.0125 \pm 0.0074	1.4587 \pm 1.4586
	Colon-IV,Traj-V	1.2547	0.3797 \pm 0.2713	0.0104 \pm 0.0063	1.1684 \pm 0.833	1.1698	0.4292 \pm 0.3302	0.0117 \pm 0.0061	1.1602 \pm 0.747
	Intestine,Traj-I	1.2028	0.3143 \pm 0.2624	0.0163 \pm 0.0067	1.2376 \pm 0.4835	0.8460	0.272 \pm 0.2502	0.0155 \pm 0.006	1.3078 \pm 0.4626
	Intestine,Traj-IV	1.0557	0.396 \pm 0.3442	0.0105 \pm 0.0069	1.0023 \pm 0.7259	0.8265	0.1464 \pm 0.1282	0.0121 \pm 0.0067	1.1546 \pm 0.7512
	Stomach-III,Traj-I	1.1392	0.2523 \pm 0.2329	0.0103 \pm 0.0072	0.8988 \pm 0.8815	1.1621	0.129 \pm 0.1042	0.0149 \pm 0.006	1.1647 \pm 0.4045
Model-III	Stomach-III,Traj-II	1.2948	0.2481 \pm 0.2218	0.011 \pm 0.0075	1.1321 \pm 1.124	1.3883	0.1424 \pm 0.1246	0.0154 \pm 0.0055	1.298 \pm 0.4613
	Colon-IV,Traj-I	0.4286	0.1651 \pm 0.1377	0.1981 \pm 0.0857	11.5582 \pm 3.0649	0.6785	0.1656 \pm 0.1365	0.1356 \pm 0.0255	9.532 \pm 2.8295
	Colon-IV,Traj-V	1.2547	0.3161 \pm 0.1926	0.0954 \pm 0.097	5.9081 \pm 4.834	1.1698	0.2077 \pm 0.1589	0.0659 \pm 0.0398	4.5974 \pm 2.8391
	Intestine,Traj-I	1.2028	2.9977 \pm 2.0789	0.3523 \pm 0.4329	11.875 \pm 3.4339	0.8460	2.2395 \pm 2.1585	0.279 \pm 0.3702	9.879 \pm 2.7667
	Intestine,Traj-IV	1.0557	0.4103 \pm 0.3641	0.0946 \pm 0.1372	5.1439 \pm 5.0448	0.8265	0.3774 \pm 0.3002	0.0898 \pm 0.1213	4.9638 \pm 3.7948
	Stomach-III,Traj-I	1.1392	0.4037 \pm 0.3949	0.0968 \pm 0.2333	4.4181 \pm 4.5253	1.1621	1.5948 \pm 1.348	0.3548 \pm 0.6203	9.894 \pm 2.2081
Model-III	Stomach-III,Traj-II	1.2948	0.9065 \pm 0.7599	0.1295 \pm 0.287	4.8385 \pm 4.3881	1.3883	0.8913 \pm 0.6449	0.3888 \pm 0.5586	10.777 \pm 3.1649

TABLE XII: **Fish-Eye Distortion.** SC-SfMLearner [33] results on three different organs and six trajectories are given for the radially distorted HighCam images for six different distortion constant, $\mu=1, 0.8, 0.7, 0.6, 0.5, 0.25$ in terms of (ATE), Translational and Rotational Relative Pose Error (RPE). We cannot derive the strong correlation between fisheye distortion level and ATE for Model-I which is fully trained with ex-vivo images.

Organ, Trajectory		Trajectory Length [m]	ATE (mean \pm std) [m]	Trans. RPE (mean \pm std) [m]	Rot. RPE (mean \pm std) [deg]	ATE (mean \pm std) [m]	Trans RPE (mean \pm std) [m]	Rot RPE (mean \pm std) [deg]
Model-I			Level-I			Level-II		
	Colon-IV,Traj-I	0.4286	0.1866 \pm 0.1827	0.0068 \pm 0.0079	4.361 \pm 4.1776	0.232 \pm 0.2292	0.0076 \pm 0.0102	4.4057 \pm 3.6682
	Colon-IV,Traj-V	1.2547	0.3912 \pm 0.2685	0.0133 \pm 0.0191	6.2669 \pm 4.016	0.4036 \pm 0.2976	0.0139 \pm 0.0194	6.6329 \pm 3.8005
	Intestine,Traj-I	1.2028	1.4841 \pm 1.3188	0.0154 \pm 0.0317	4.4296 \pm 3.8034	1.1338 \pm 0.8529	0.0159 \pm 0.0325	4.6956 \pm 3.8903
	Intestine,Traj-IV	1.0557	1.0085 \pm 0.7939	0.0104 \pm 0.0172	5.2256 \pm 4.7665	1.0157 \pm 0.8167	0.0109 \pm 0.0184	5.3752 \pm 4.5575
	Stomach-III,Traj-I	1.1391	0.4456 \pm 0.4905	0.01 \pm 0.0193	4.431 \pm 4.1757	0.3577 \pm 0.3426	0.0103 \pm 0.0186	4.7135 \pm 4.3592
Model-I	Stomach-III,Traj-II	1.2948	0.7703 \pm 0.654	0.0132 \pm 0.025	5.0163 \pm 4.5857	0.745 \pm 0.5999	0.0136 \pm 0.0251	5.3127 \pm 4.6194
			Level-III			Level-IV		
	Colon-IV,Traj-I	0.4286	0.2239 \pm 0.2154	0.0081 \pm 0.0114	4.494 \pm 3.4739	0.2283 \pm 0.2008	0.0087 \pm 0.0126	4.6566 \pm 3.4325
	Colon-IV,Traj-V	1.2547	0.1889 \pm 0.165	0.011 \pm 0.0134	5.7492 \pm 4.0122	0.2935 \pm 0.2277	0.0119 \pm 0.0155	5.9168 \pm 4.0263
	Intestine,Traj-I	1.2028	1.8414 \pm 1.7606	0.0162 \pm 0.033	4.7988 \pm 3.7923	1.78 \pm 1.8947	0.0163 \pm 0.0328	4.9426 \pm 3.7293
	Intestine,Traj-IV	1.0557	0.9971 \pm 0.812	0.0111 \pm 0.0192	5.444 \pm 4.3981	0.9964 \pm 0.84	0.0013 \pm 0.0197	5.5487 \pm 4.2526
Model-I	Stomach-III,Traj-I	1.1391	0.5615 \pm 0.5029	0.0106 \pm 0.0195	4.8433 \pm 4.4158	0.8088 \pm 0.6818	0.0109 \pm 0.0194	4.9711 \pm 4.4473
	Stomach-III,Traj-II	1.2948	0.5947 \pm 0.4583	0.0135 \pm 0.0251	5.4708 \pm 4.6777	0.3759 \pm 0.3313	0.0137 \pm 0.0251	5.6405 \pm 4.6773
			Level-V			Level-VI		
	Colon-IV,Traj-I	0.4286	0.1723 \pm 0.1294	0.0094 \pm 0.0135	4.9048 \pm 3.4492	0.1734 \pm 0.1819	0.0106 \pm 0.0124	5.958 \pm 3.2239
	Colon-IV,Traj-V	1.2547	0.3169 \pm 0.2379	0.0129 \pm 0.0181	6.1531 \pm 4.0592	0.444 \pm 0.3631	0.0143 \pm 0.0199	6.7759 \pm 3.7336
	Intestine,Traj-I	1.2028	1.4362 \pm 1.4126	0.0165 \pm 0.0327	5.189 \pm 3.8098	0.7182 \pm 0.8163	0.0154 \pm 0.0261	5.8362 \pm 3.1785
Model-I	Intestine,Traj-IV	1.0557	0.8902 \pm 0.7819	0.0113 \pm 0.019	5.6253 \pm 3.9955	0.7663 \pm 0.5972	0.0112 \pm 0.0147	6.0696 \pm 3.3439
	Stomach-III,Traj-I	1.1391	0.854 \pm 0.7009	0.0112 \pm 0.0197	5.0878 \pm 4.3951	0.4324 \pm 0.3413	0.0121 \pm 0.0183	5.7232 \pm 3.9662
	Stomach-III,Traj-II	1.2948	0.256 \pm 0.2451	0.0138 \pm 0.0235	5.8396 \pm 4.7512	0.2175 \pm 0.2062	0.0138 \pm 0.0198	6.2993 \pm 4.235

Organ, Trajectory		Trajectory Length [m]	ATE (mean± std) [m]	Trans. RPE (mean± std) [m]	Rot. RPE (mean± std) [deg]	ATE (mean± std) [m]	Trans RPE (mean± std) [m]	Rot RPE (mean± std) [deg]
Model-I			Level-I			Level-II		
	Colon-IV,Traj-I	0.4286	0.5189± 0.4899	0.0085± 0.0123	5.313± 6.7259	0.4695± 0.4403	0.0083± 0.0115	5.364± 6.7648
	Colon-IV,Traj-V	1.2547	0.778± 0.4805	0.0125± 0.0208	6.0845± 6.2872	0.6343± 0.4146	0.0121± 0.0185	6.1295± 6.2838
	Intestine,Traj-I	1.2028	4.9987± 4.2305	0.0253± 0.0587	5.3764± 6.3418	4.6303± 4.1459	0.0245± 0.057	5.4155± 6.3404
	Intestine,Traj-IV	1.0557	2.1009± 1.6748	0.0167± 0.0318	6.6196± 8.0138	2.2758± 1.8579	0.0163± 0.031	6.6885± 8.0452
	Stomach-III,Traj-I	1.1391	1.2179± 1.1963	0.0162± 0.037	4.6951± 5.0168	1.0687± 1.04672	0.0156± 0.0353	4.7896± 5.099
	Stomach-III,Traj-II	1.2948	1.569± 1.5046	0.0217± 0.0468	5.5896± 6.277	1.3861± 1.2372	0.021± 0.0445	5.6839± 6.3662
Model-I			Level-III			Level-IV		
	Colon-IV,Traj-I	0.4286	0.4498± 0.4208	0.0082± 0.0112	5.3815± 6.7567	0.4137± 0.386	0.0081± 0.0107	5.4093± 6.7185
	Colon-IV,Traj-V	1.2547	0.5899± 0.4119	0.0119± 0.0179	6.1502± 6.2691	0.4745± 0.3731	0.0117± 0.0167	6.196± 6.2337
	Intestine,Traj-I	1.2028	4.4718± 4.0515	0.0241± 0.0563	5.4369± 6.3341	4.3406± 3.9633	0.0234± 0.0551	5.484± 6.3321
	Intestine,Traj-IV	1.0557	2.3599± 1.9431	0.0161± 0.0307	6.7134± 8.0463	2.46± 2.0519	0.0158± 0.0302	6.7587± 8.0479
	Stomach-III,Traj-I	1.1391	1.0081± 0.987	0.0154± 0.0347	4.8232± 5.1255	0.8982± 0.8529	0.0151± 0.0336	4.8891± 5.1787
	Stomach-III,Traj-II	1.2948	1.3448± 1.1728	0.0208± 0.0437	5.7183± 6.3959	1.2716± 1.069	0.0203± 0.0421	5.7859± 6.4462
Model-I			Level-V			Level-VI		
	Colon-IV,Traj-I	0.4286	0.3672± 0.3408	0.008± 0.0101	5.4441± 6.6404	0.3434± 0.3177	0.0079± 0.0098	5.4576± 6.582
	Colon-IV,Traj-V	1.2547	0.3117± 0.3037	0.0114± 0.0154	6.2775± 6.1912	0.3127± 0.3026	0.0113± 0.0148	6.3284± 6.1642
	Intestine,Traj-I	1.2028	4.1963± 3.7985	0.0224± 0.0532	5.5473± 6.3178	3.9369± 3.4844	0.0219± 0.0521	5.583± 6.3083
	Intestine,Traj-IV	1.0557	2.4921± 2.1067	0.0154± 0.0293	6.8282± 8.0545	2.4589± 2.0925	0.0151± 0.0285	6.8633± 8.0423
	Stomach-III,Traj-I	1.1391	0.7528± 0.6885	0.0146± 0.032	4.9739± 5.239	0.6841± 0.6623	0.0144± 0.0311	5.0284± 5.2814
	Stomach-III,Traj-II	1.2948	1.2044± 0.977	0.0197± 0.0398	5.88± 6.5087	1.1854± 0.9502	0.0193± 0.0385	5.9369± 6.5435

TABLE XIV: **Fish-Eye Distortion.** SC-SfMLearner results on two trajectories of three different organs are given for the radially distorted HighCam images for six different distortion constant, $\mu=1, 0.8, 0.7, 0.6, 0.5, 0.25$ in terms of (ATE), Translational and Rotational Relative Pose Error (RPE). Model-II shows results of training the same model via synthetic data generated in Unity simulation environment. Model-III is the fine-tuned version of Unity trained model with the various trajectories from three different organs.

Organ, Trajectory		Trajectory Length [m]	ATE (mean \pm std) [m]	Trans. RPE (mean \pm std) [m]	Rot. RPE (mean \pm std) [deg]	ATE (mean \pm std) [m]	Trans RPE (mean \pm std) [m]	Rot RPE (mean \pm std) [deg]
Model-I			Level-I			Level-II		
	Colon-IV,Traj-I	0.4286	0.2004 \pm 0.1929	0.0014 \pm 0.0028	0.9996 \pm 0.6575	0.2122 \pm 0.2028	0.0014 \pm 0.0028	1.0749 \pm 0.6891
	Colon-IV,Traj-V	1.2547	0.4222 \pm 0.3006	0.0019 \pm 0.002	1.1573 \pm 0.7841	0.4342 \pm 0.3036	0.002 \pm 0.002	1.1864 \pm 0.7816
	Intestine,Traj-I	1.2028	0.165 \pm 0.147	0.0014 \pm 0.0009	1.0798 \pm 0.6945	0.1629 \pm 0.112	0.0014 \pm 0.0009	1.1827 \pm 0.72
	Intestine,Traj-IV	1.0557	0.42 \pm 0.3651	0.0016 \pm 0.0013	1.0302 \pm 0.6778	0.4275 \pm 0.3636	0.0017 \pm 0.0013	1.1094 \pm 0.6995
	Stomach-III,Traj-I	1.1391	0.2446 \pm 0.2136	0.0018 \pm 0.0024	0.9553 \pm 0.8891	0.2035 \pm 0.16	0.0018 \pm 0.0024	1.0122 \pm 0.9114
Model-II	Stomach-III,Traj-II	1.2948	0.2729 \pm 0.2267	0.0022 \pm 0.0038	1.1725 \pm 1.1082	0.2705 \pm 0.2086	0.0022 \pm 0.0038	1.2166 \pm 1.1164
			Level-III			Level-IV		
	Colon-IV,Traj-I	0.4286	0.2195 \pm 0.2107	0.0015 \pm 0.0028	1.1112 \pm 0.6891	0.2066 \pm 0.1941	0.0015 \pm 0.0028	1.1243 \pm 0.6797
	Colon-IV,Traj-V	1.2547	0.4125 \pm 0.2877	0.002 \pm 0.002	1.2011 \pm 0.7884	0.3851 \pm 0.2795	0.002 \pm 0.002	1.2052 \pm 0.7781
	Intestine,Traj-I	1.2028	0.1932 \pm 0.149	0.0015 \pm 0.0009	1.2253 \pm 0.7217	0.2535 \pm 0.202	0.0015 \pm 0.0009	1.2606 \pm 0.7149
	Intestine,Traj-IV	1.0557	0.4184 \pm 0.3518	0.0017 \pm 0.0013	1.1484 \pm 0.6976	0.3815 \pm 0.3167	0.0017 \pm 0.0013	1.1795 \pm 0.6988
Model-III	Stomach-III,Traj-I	1.1391	0.1835 \pm 0.1353	0.0018 \pm 0.0024	1.0342 \pm 0.9148	0.156 \pm 0.1177	0.0018 \pm 0.0024	1.049 \pm 0.9219
	Stomach-III,Traj-II	1.2948	0.2626 \pm 0.2006	0.0022 \pm 0.0038	1.2494 \pm 1.1265	0.245 \pm 0.1842	0.0022 \pm 0.0038	1.2693 \pm 1.1329
			Level-V			Level-VI		
	Colon-IV,Traj-I	0.4286	0.1856 \pm 0.167	0.0016 \pm 0.0028	1.1166 \pm 0.6624	0.1109 \pm 0.0953	0.0016 \pm 0.0028	1.0636 \pm 0.6017
	Colon-IV,Traj-V	1.2547	0.3727 \pm 0.264	0.0021 \pm 0.002	1.2062 \pm 0.7662	0.3781 \pm 0.2377	0.0021 \pm 0.002	1.141 \pm 0.683
	Intestine,Traj-I	1.2028	0.3356 \pm 0.2763	0.0016 \pm 0.0009	1.2707 \pm 0.6904	0.4794 \pm 0.3441	0.0017 \pm 0.0008	1.1977 \pm 0.6185
Model-III	Intestine,Traj-IV	1.0557	0.3244 \pm 0.2676	0.0017 \pm 0.0013	1.1942 \pm 0.6808	0.2506 \pm 0.2126	0.0019 \pm 0.0013	1.1288 \pm 0.5978
	Stomach-III,Traj-I	1.1391	0.155 \pm 0.1234	0.0018 \pm 0.0024	1.0719 \pm 0.92	0.2142 \pm 0.1694	0.0019 \pm 0.0025	1.0467 \pm 0.8751
	Stomach-III,Traj-II	1.2948	0.2389 \pm 0.1721	0.0023 \pm 0.0038	1.2767 \pm 1.1264	0.2326 \pm 0.1738	0.0023 \pm 0.0038	1.2305 \pm 1.0637
			Level-I			Level-II		
	Colon-IV,Traj-I	0.4286	0.1434 \pm 0.1187	0.0696 \pm 0.0691	4.4131 \pm 3.96	0.1676 \pm 0.1434	0.0723 \pm 0.0711	4.6129 \pm 3.8267
	Colon-IV,Traj-V	1.2546	0.3913 \pm 0.3049	0.0939 \pm 0.1008	5.6239 \pm 4.5886	0.3908 \pm 0.3245	0.1036 \pm 0.127	5.8188 \pm 4.3038
Model-III	Intestine,Traj-I	1.2028	1.306 \pm 1.1803	0.1612 \pm 0.4112	4.8132 \pm 4.2146	2.1595 \pm 2.1824	0.1664 \pm 0.4305	5.0356 \pm 4.1821
	Intestine,Traj-IV	1.0557	0.5452 \pm 0.4657	0.0975 \pm 0.1401	5.1394 \pm 4.3576	0.593 \pm 0.5006	0.0986 \pm 0.1419	5.2657 \pm 4.159
	Stomach-III,Traj-I	1.1391	0.3618 \pm 0.3986	0.0988 \pm 0.225	4.5224 \pm 4.3248	0.319 \pm 0.3358	0.1011 \pm 0.2287	4.7846 \pm 4.4399
	Stomach-III,Traj-II	1.2948	0.8732 \pm 0.6381	0.1294 \pm 0.2833	5.0621 \pm 4.4338	0.7969 \pm 0.5784	0.1301 \pm 0.2932	5.4049 \pm 4.6375
			Level-III			Level-IV		
	Colon-IV,Traj-I	0.4286	0.1792 \pm 0.1557	0.0747 \pm 0.076	4.7197 \pm 3.7331	0.1927 \pm 0.1677	0.0778 \pm 0.0842	4.8911 \pm 3.744
Model-III	Colon-IV,Traj-V	1.2547	0.3447 \pm 0.2734	0.1096 \pm 0.1429	5.9395 \pm 4.1783	0.3689 \pm 0.2464	0.1169 \pm 0.1652	6.1216 \pm 4.1345
	Intestine,Traj-I	1.2028	2.0558 \pm 2.1545	0.1688 \pm 0.4392	5.1351 \pm 4.122	1.0973 \pm 1.1361	0.1716 \pm 0.4398	5.3066 \pm 4.1896
	Intestine,Traj-IV	1.0557	0.457 \pm 0.369	0.0967 \pm 0.1282	5.3725 \pm 4.1259	0.3321 \pm 0.2694	0.094 \pm 0.1154	5.4286 \pm 3.997
	Stomach-III,Traj-I	1.1391	0.3677 \pm 0.3582	0.1028 \pm 0.234	4.9334 \pm 4.5316	0.6718 \pm 0.6501	0.1057 \pm 0.2458	5.0679 \pm 4.5506
	Stomach-III,Traj-II	1.2948	0.6772 \pm 0.5306	0.1298 \pm 0.2935	5.603 \pm 4.7666	0.4219 \pm 0.3422	0.1282 \pm 0.2785	5.7873 \pm 4.8586
			Level-V			Level-VI		
Model-III	Colon-IV,Traj-I	0.4286	0.1573 \pm 0.1397	0.0844 \pm 0.1044	5.0893 \pm 3.7228	0.1816 \pm 0.155	0.087 \pm 0.0743	5.5718 \pm 3.6608
	Colon-IV,Traj-V	1.2547	0.4281 \pm 0.3078	0.1273 \pm 0.2071	6.3029 \pm 4.081	0.7969 \pm 0.3952	0.1354 \pm 0.2505	6.6467 \pm 3.9828
	Intestine,Traj-I	1.2028	1.5151 \pm 1.4755	0.1743 \pm 0.4484	5.4191 \pm 3.9895	1.303 \pm 1.2469	0.1356 \pm 0.2793	5.911 \pm 3.7903
	Intestine,Traj-IV	1.0557	0.3202 \pm 0.2924	0.0908 \pm 0.0927	5.5059 \pm 3.8728	0.2188 \pm 0.1991	0.0838 \pm 0.0664	5.5075 \pm 3.5455
	Stomach-III,Traj-I	1.1391	0.8671 \pm 0.8955	0.1066 \pm 0.2304	5.2224 \pm 4.6073	0.5023 \pm 0.3686	0.0969 \pm 0.1516	5.4002 \pm 4.4628
	Stomach-III,Traj-II	1.2948	0.3095 \pm 0.2476	0.1267 \pm 0.2511	5.9604 \pm 4.9215	0.2289 \pm 0.2266	0.1197 \pm 0.1963	6.1122 \pm 4.8741

TABLE XV: **Gaussian-Blur.** SC-SfMLearner results on three different organs and six trajectories are given for the HighCam images with the Gaussian-Blur effect added for six different distortion constant, $\alpha = (5,11,13,17,23,27)$, $\beta = (5,50,100,110,120,150)$ and $\gamma = (5,7,10,20,40,80)$, in terms of (ATE), Translational and Rotational Relative Pose Error (RPE).

Organ, Trajectory		Trajectory Length [m]	ATE (mean \pm std) [m]	Trans. RPE (mean \pm std) [m]	Rot. RPE (mean \pm std) [deg]	ATE (mean \pm std) [m]	Trans RPE (mean \pm std) [m]	Rot RPE (mean \pm std) [deg]
Model-I			Level-I			Level-II		
	Colon-IV,Traj-I	0.4286	0.1686 \pm 0.1507	0.0013 \pm 0.0028	1.0082 \pm 0.7035	0.187 \pm 0.1637	0.0013 \pm 0.0028	1.0486 \pm 0.7198
	Colon-IV,Traj-V	1.2547	0.3534 \pm 0.2465	0.0019 \pm 0.002	1.202 \pm 0.8419	0.384 \pm 0.2678	0.0019 \pm 0.002	1.2782 \pm 0.8709
	Intestine,Traj-I	1.2028	0.2011 \pm 0.163	0.0014 \pm 0.0009	1.0341 \pm 0.7125	0.2137 \pm 0.1912	0.0014 \pm 0.001	1.0941 \pm 0.7233
	Intestine,Traj-IV	1.0557	0.377 \pm 0.3283	0.0016 \pm 0.0013	1.0228 \pm 0.7406	0.401 \pm 0.3445	0.0017 \pm 0.0013	1.0698 \pm 0.7692
	Stomach-III,Traj-I	1.1391	0.1888 \pm 0.1707	0.0018 \pm 0.0024	0.9066 \pm 0.8964	0.2242 \pm 0.2031	0.0019 \pm 0.0024	0.9285 \pm 0.8965
Model-II	Stomach-III,Traj-II	1.2948	0.2173 \pm 0.2027	0.0022 \pm 0.0038	1.1545 \pm 1.1388	0.2297 \pm 0.204	0.0022 \pm 0.0038	1.1896 \pm 1.1366
			Level-III			Level-IV		
	Colon-IV,Traj-I	0.4286	0.1919 \pm 0.1673	0.0013 \pm 0.0028	1.0503 \pm 0.7106	0.1944 \pm 0.1654	0.0014 \pm 0.0028	1.0531 \pm 0.6906
	Colon-IV,Traj-V	1.2547	0.3912 \pm 0.2718	0.0019 \pm 0.002	1.2928 \pm 0.8727	0.391 \pm 0.2659	0.0019 \pm 0.002	1.3113 \pm 0.87
	Intestine,Traj-I	1.2028	0.2172 \pm 0.1956	0.0015 \pm 0.001	1.1078 \pm 0.7212	0.2185 \pm 0.2021	0.0015 \pm 0.001	1.1315 \pm 0.7124
	Intestine,Traj-IV	1.0557	0.4047 \pm 0.3484	0.0017 \pm 0.0013	1.0776 \pm 0.7698	0.4016 \pm 0.349	0.0017 \pm 0.0013	1.0951 \pm 0.7633
Model-III	Stomach-III,Traj-I	1.1391	0.2346 \pm 0.2131	0.0019 \pm 0.0024	1.0951 \pm 0.8943	0.2503 \pm 0.2283	0.0019 \pm 0.0024	0.9481 \pm 0.8914
	Stomach-III,Traj-II	1.2948	0.2232 \pm 0.2051	0.0022 \pm 0.0038	1.197 \pm 1.1309	0.2384 \pm 0.2055	0.0022 \pm 0.0038	1.2081 \pm 1.1202
			Level-V			Level-VI		
	Colon-IV,Traj-I	0.4286	0.183 \pm 0.1444	0.0014 \pm 0.0028	1.0858 \pm 0.6624	0.1755 \pm 0.1307	0.0014 \pm 0.0028	1.1227 \pm 0.6484
	Colon-IV,Traj-V	1.2547	0.3676 \pm 0.241	0.0019 \pm 0.002	1.3318 \pm 0.8513	0.3425 \pm 0.2224	0.0019 \pm 0.002	1.3447 \pm 0.8372
	Intestine,Traj-I	1.2028	0.2179 \pm 0.2092	0.0015 \pm 0.001	1.1656 \pm 0.7029	0.2124 \pm 0.1986	0.0015 \pm 0.001	1.1878 \pm 0.7019
Model-IV	Intestine,Traj-IV	1.0557	0.4017 \pm 0.3524	0.0017 \pm 0.0013	1.1313 \pm 0.746	0.4153 \pm 0.3642	0.0017 \pm 0.0013	1.1565 \pm 0.7312
	Stomach-III,Traj-I	1.1391	0.2631 \pm 0.2407	0.0019 \pm 0.0024	0.974 \pm 0.8933	0.2623 \pm 0.2398	0.0019 \pm 0.0024	0.9918 \pm 0.8983
	Stomach-III,Traj-II	1.2948	0.2427 \pm 0.2015	0.0022 \pm 0.0038	1.2231 \pm 1.1037	0.243 \pm 0.1976	0.0022 \pm 0.0038	1.2304 \pm 1.0966
			Level-I			Level-II		
	Colon-IV,Traj-I	0.4286	0.2591 \pm 0.2349	0.0099 \pm 0.0155	4.6258 \pm 5.1319	0.2708 \pm 0.2458	0.0099 \pm 0.0152	4.669 \pm 5.1285
	Colon-IV,Traj-V	1.2547	1.1798 \pm 0.7551	0.0121 \pm 0.0167	6.3819 \pm 6.8848	1.1264 \pm 0.7199	0.0119 \pm 0.0159	6.5266 \pm 7.0337
Model-V	Intestine,Traj-I	1.2028	6.7507 \pm 5.98429	0.0262 \pm 0.0618	5.7217 \pm 6.8992	4.4069 \pm 3.0129	0.0255 \pm 0.0601	5.8384 \pm 6.9854
	Intestine,Traj-IV	1.0557	0.5968 \pm 0.4954	0.0159 \pm 0.0303	6.1581 \pm 7.4983	0.6812 \pm 0.6214	0.0155 \pm 0.0288	6.2861 \pm 7.6739
	Stomach-III,Traj-I	1.1391	0.778 \pm 0.747	0.0136 \pm 0.031	5.1267 \pm 6.1877	0.7944 \pm 0.7859	0.0135 \pm 0.0305	5.2286 \pm 6.327
	Stomach-III,Traj-II	1.2948	1.1846 \pm 0.8342	0.0194 \pm 0.0438	5.3206 \pm 5.2819	1.0467 \pm 0.7738	0.0192 \pm 0.043	5.4121 \pm 5.4038
			Level-III			Level-IV		
	Colon-IV,Traj-I	0.4286	0.2738 \pm 0.2488	0.0099 \pm 0.015	4.6841 \pm 5.1123	0.2827 \pm 0.2576	0.0099 \pm 0.0147	4.7194 \pm 5.0787
Model-VI	Colon-IV,Traj-V	1.2547	1.0958 \pm 0.6967	0.0118 \pm 0.0156	6.5699 \pm 7.0556	1.0302 \pm 0.6418	0.0117 \pm 0.015	6.6518 \pm 7.0825
	Intestine,Traj-I	1.2028	4.0995 \pm 02.7416	0.0252 \pm 0.0591	5.8836 \pm 6.9945	3.9276 \pm 2.7603	0.0245 \pm 0.057	5.9555 \pm 6.9725
	Intestine,Traj-IV	1.0557	0.726 \pm 0.6688	0.0154 \pm 0.0283	6.3263 \pm 7.7141	0.7873 \pm 0.7183	0.0151 \pm 0.0272	6.3981 \pm 7.7819
	Stomach-III,Traj-I	1.1391	0.7839 \pm 0.7806	0.0134 \pm 0.0301	5.267 \pm 6.3662	0.7392 \pm 0.7387	0.0133 \pm 0.0294	5.337 \pm 6.413
	Stomach-III,Traj-II	1.2948	1.0461 \pm 0.7655	0.0192 \pm 0.0428	5.4493 \pm 5.4422	1.0914 \pm 0.7607	0.019 \pm 0.0421	5.5257 \pm 5.5164
			Level-V			Level-VI		
Model-VII	Colon-IV,Traj-I	0.4286	0.2975 \pm 0.2706	0.0099 \pm 0.0141	4.7812 \pm 5.0524	0.2971 \pm 0.2702	0.0098 \pm 0.0137	4.8285 \pm 5.0696
	Colon-IV,Traj-V	1.2547	0.9082 \pm 0.5515	0.0116 \pm 0.0144	6.7562 \pm 7.0636	0.81 \pm 0.4938	0.0116 \pm 0.014	6.8068 \pm 7.0113
	Intestine,Traj-I	1.2028	3.6059 \pm 2.7179	0.0235 \pm 0.0541	6.0239 \pm 6.8804	3.3098 \pm 2.5554	0.0229 \pm 0.0526	6.0511 \pm 6.8195
	Intestine,Traj-IV	1.0557	0.8074 \pm 0.7112	0.0147 \pm 0.0258	6.4829 \pm 7.8067	0.7845 \pm 0.6714	0.0145 \pm 0.0252	6.5223 \pm 7.78
	Stomach-III,Traj-I	1.1391	0.6149 \pm 0.6018	0.013 \pm 0.0278	5.4429 \pm 6.4698	0.5489 \pm 0.5389	0.0128 \pm 0.0268	5.5097 \pm 6.4967
	Stomach-III,Traj-II	1.2948	1.2358 \pm 0.8664	0.0188 \pm 0.0409	5.6598 \pm 5.6672	1.3317 \pm 0.99	0.0187 \pm 0.0402	5.7456 \pm 5.7714

APPENDIX H. STATISTICAL ANALYSIS

TABLE XVI: **Wilcoxon Signed Rank Test for Gaussian Blur Effect.** Model performances are compared for six level of Gaussian blurring effect with parameter set $\alpha = (5, 11, 13, 17, 23, 27)$, $\beta = (5, 50, 100, 110, 120, 150)$ and $\gamma = (5, 7, 10, 20, 40, 80)$, respectively. We split the previously used test trajectories of Colon-IV, Small Intestine and Stomach-III evenly until getting 20 test sub-trajectories. We presented the results for the analogized levels of those test groups. We do not observe any p-value less than 0.05 in terms of ATE for all models. However, Model-II performs significantly different ($p < 0.05$) on first degradation level compared to sixth and fifth degradation level in terms of rotational error.

Effect Levels	ATE(mean)[m] p-value	Rot. RPE[deg] p-value	ATE(mean)[m] p-value	Rot. RPE[deg] p-value	ATE(mean)[m] p-value	Rot. RPE[deg] p-value
	Model-I		Model-II		Model-III	
Level I - Level II	0.347	0.388	0.237	0.168	0.420	0.228
Level I - Level III	0.308	0.368	0.245	0.128	0.409	0.162
Level I - Level IV	0.237	0.280	0.220	0.082	0.378	0.109
Level I - Level V	0.205	0.228	0.237	0.019	0.409	0.078
Level I - Level VI	0.168	0.190	0.271	0.010	0.290	0.057
Level II - Level III	0.388	0.378	0.378	0.357	0.430	0.308
Level II - Level IV	0.308	0.328	0.378	0.271	0.425	0.182
Level II - Level V	0.245	0.245	0.399	0.099	0.430	0.125
Level II - Level VI	0.190	0.237	0.452	0.070	0.328	0.137
Level III - Level IV	0.318	0.328	0.378	0.318	0.462	0.245
Level III - Level V	0.280	0.262	0.484	0.131	0.409	0.149
Level III - Level VI	0.220	0.237	0.484	0.078	0.318	0.149
Level IV - Level V	0.338	0.318	0.495	0.237	0.388	0.228
Level IV - Level VI	0.299	0.271	0.484	0.149	0.308	0.197
Level V - Level VI	0.409	0.338	0.495	0.357	0.338	0.347

TABLE XVII: **Wilcoxon Signed Rank Test for Fish-Eye Effect.** Model-I, Model-II and Model-III performances are compared for six level fish eye distortion with $\mu = 1, 0.8, 0.7, 0.6, 0.5, 0.25$. For Model-II, increasing distortion differences between compared groups result in decreasing p-values for absolute trajectory error as expected. Whereas, Model-I and Model-III which are trained by dataset including ex-vivo endoscopy images do not show the same tendency. Despite the fact that no statistical significance is achieved in terms of ATE on all distorted levels, we observe $p < 0.05$ for rotational RPE.

Effect Levels	ATE(mean)[m] p-value	Rot. RPE[deg] p-value	ATE(mean)[m] p-value	Rot. RPE[deg] p-value	ATE(mean)[m] p-value	Rot. RPE[deg] p-value
	Model-I		Model-II		Model-III	
Level I - Level II	0.452	0.162	0.430	0.022	0.441	0.120
Level I - Level III	0.441	0.162	0.378	0.002	0.420	0.023
Level I - Level IV	0.399	0.062	0.338	0.001	0.149	0.023
Level I - Level V	0.262	0.025	0.290	0.00001	0.290	0.008
Level I - Level VI	0.032	0.00001	0.228	0.004	0.228	0.002
Level II - Level III	0.420	0.357	0.399	0.165	0.357	0.074
Level II - Level IV	0.462	0.212	0.357	0.043	0.152	0.045
Level II - Level V	0.262	0.095	0.347	0.032	0.262	0.011
Level II - Level VI	0.036	0.001	0.197	0.452	0.193	0.002
Level III - Level IV	0.495	0.190	0.393	0.212	0.228	0.299
Level III - Level V	0.318	0.054	0.373	0.168	0.328	0.090
Level III - Level VI	0.082	0.0001	0.262	0.155	0.299	0.018
Level IV - Level V	0.308	0.182	0.388	0.420	0.484	0.125
Level IV - Level VI	0.054	0.00001	0.276	0.043	0.399	0.014
Level V - Level VI	0.137	0.002	0.420	0.023	0.308	0.057